

1 **Beyond Binary Maps from HCHO/NO<sub>2</sub>: A Deep Neural Network**  
2 **Approach to Global Daily Mapping of Net Ozone Production Rates**  
3 **and Sensitivities Constrained by Satellite Observations (2005–2023)**

5 **Amir H. Souri<sup>1,2\*</sup>, Gonzalo González Abad<sup>3</sup>, Bryan N. Duncan<sup>1</sup>, Luke D. Oman<sup>1</sup>**

6 <sup>1</sup>Atmospheric Chemistry and Dynamics Laboratory, NASA Goddard Space Flight Center, Greenbelt, MD,  
7 USA

8 <sup>2</sup>GESTAR II, Morgan State University, Baltimore, MD, USA

9 <sup>3</sup>Atomic and Molecular Physics (AMP) Division, Center for Astrophysics | Harvard & Smithsonian,  
10 Cambridge, MA, USA

11 \* Corresponding author: [a.souri@nasa.gov](mailto:a.souri@nasa.gov)

12 **Abstract.** Previous studies on net ozone production rates (PO<sub>3</sub>) and their sensitivities to precursors relied  
13 on limited in-situ data, often coarse and uncertain chemical transport models (CTMs), and ozone indicators  
14 like the formaldehyde-to-nitrogen dioxide ratio (FNR). However, FNR fails to fully capture PO<sub>3</sub>'s complex  
15 relationships with pollution, light, and water vapor. To address this, we refine the satellite-based PO<sub>3</sub>  
16 product from Souri et al. (2025) with key advancements: (i) a deep neural network to parametrize high-  
17 dimensional non-linear ozone chemistry without the need for empirical linearization of atmospheric  
18 conditions, (ii) incorporation of water vapor, (iii) improved error characterization, and (iv) the application  
19 of a finer CTM to dynamically convert column retrievals into near-surface mixing ratios. Our PO<sub>3</sub>  
20 sensitivity maps surpass traditional FNR-based assessments by quantifying sensitivity magnitudes –  
21 factoring in photolysis rates and water vapor – with greater spatial information. Our new product provides  
22 daily near-clear sky PO<sub>3</sub> and sensitivity maps using bias-corrected OMI (2005–2019, 0.25° × 0.25°) and  
23 TROPOMI (2018–2023, 0.1° × 0.1°), with values aligning within 10%. High PO<sub>3</sub> rates (>8 ppbv/hr) appear  
24 in urban and biomass-burning regions under strong photochemical activity, including during a heatwave in  
25 the northeastern U.S. Photolysis rates are the dominant factor dictating the seasonality of PO<sub>3</sub> magnitudes  
26 and sensitivities. The stability and long-term records of OMI retrievals (2005–2019) enable us to provide  
27 the first global maps of PO<sub>3</sub> linear trends showing a surge of >30% over China, the Middle East, and India,  
28 while a reduction in the eastern U.S., southern Europe, and several regions in Africa.

29 **1. Introduction.**

30 To mitigate tropospheric ozone pollution, a pervasive trace gas that impacts human health, climate,  
31 and crop productivity (Fleming et al., 2018; Mills et al., 2018; Gaudel et al., 2018), it is essential to quantify  
32 the spatiotemporal variations of two primary components: i) the sensitivity of the chemical net production  
33 rates of ozone (PO<sub>3</sub>) to its two main precursors, nitrogen oxides (NO<sub>x</sub>=NO+NO<sub>2</sub>) and volatile organic  
34 compounds (VOCs), and ii) the magnitude of PO<sub>3</sub> itself. The first component provides insights into the  
35 positive and negative contributions of these precursors to PO<sub>3</sub>, which are typically categorized as NO<sub>x</sub>-  
36 sensitive (where PO<sub>3</sub> is influenced mainly by NO<sub>x</sub>), VOC-sensitive (where PO<sub>3</sub> is affected primarily by  
37 VOCs), and transitional regimes (where PO<sub>3</sub> is responsive to both NO<sub>x</sub> and VOCs) (Kleinman et al., 2002;  
38 Silman and He, 2002; Duncan et al., 2010). The latter component is crucial for understanding how locally  
39 produced ozone, in conjunction with advected or diffused ozone, can lead to high-ozone events (e.g.,  
40 Kleinman et al., 2002, 2005; Sullivan et al., 2019).

41 Creating global maps of PO<sub>3</sub> and its sensitivity at spatiotemporal scales relevant to air quality  
42 policies is a challenge. Unique instruments can directly measure PO<sub>3</sub> by calculating the difference in ozone

43 molecules from air samples drawn through two distinct tubes – one exposed to sunlight and the other  
44 shielded by an ultra-violet (UV) filter (Cazorla and Brune, 2010; Sadanaga et al., 2017; Sklaveniti et al.,  
45 2018). However, these instruments suffer from various interferences, such as heterogeneous chemistry or  
46 photo-enhanced loss of ozone within the tubes, and they are limited to sparse super sites that restrict spatial  
47 variability. Similarly, box-model simulations of  $\text{PO}_3$ , which are observationally constrained by intensive  
48 atmospheric composition measurements, are also limited by sparse aircraft sampling (Cazorla et al., 2012;  
49 Ren et al., 2013; Mazzuca et al.; 2016; Souri et al., 2020a; Schroeder et al., 2020; Brune et al., 2022; Wolfe  
50 et al., 2022; Souri et al., 2023a). Currently, our understanding of the global spatiotemporal variability of  
51  $\text{PO}_3$  mainly relies on chemical transport models, which can possess significant uncertainties such as those  
52 associated with transport, emissions, and dry deposition. Moreover, they may lack the spatial resolution  
53 necessary to capture the non-linear dynamics associated with  $\text{NO}_x$  and thus, ozone chemistry (Valin et al.,  
54 2011; Vinken et al., 2011; Yu et al., 2016).

55 The “gold standard” approach to determine three-dimensional  $\text{PO}_3$  within a process-based  
56 framework involves running a high-resolution chemical transport model, with prognostic inputs constrained  
57 by observations. This approach falls into the realm of an inversion/data assimilation framework (Bocquet  
58 et al., 2015). Numerous studies have aimed to constrain various model prognostic inputs, including  $\text{NO}_x$   
59 and VOCs emissions and/or concentrations, using aircraft and satellite remote sensing retrievals (e.g.,  
60 Stavrakou et al., 2009, 2016; Souri et al., 2016; Bauwens et al., 2016; Miyazaki et al., 2020; Opacka et al.,  
61 2025). Notably, Souri et al. (2020b) developed a non-linear joint inversion of  $\text{NO}_x$  and VOCs to better  
62 constrain  $\text{PO}_3$ , thereby shedding light on the impact of recent emission regulations in East Asia on the  
63 different chemical pathways governing the formation and loss of surface ozone. However, these studies  
64 face a fundamental challenge: discrepancies between simulated fields and observations are often blamed  
65 solely on emissions. In fact, such discrepancies can also stem from various model components, including  
66 chemical mechanisms, dry deposition, photolysis rates, vertical diffusion, and transport. Given the limited  
67 observations available for constraining all of these uncertain parameters, the optimization problem becomes  
68 grossly under-determined. This means we lack sufficient information to uniquely determine the optimal  
69 values of these parameters altogether. Additionally, the underlying physics of these models is inherently  
70 uncertain, necessitating the explicit propagation of model physics errors into our final estimates or the  
71 execution of ensemble model realizations to stochastically vet the credibility of the top-down estimates  
72 across different realizations. Conducting these ensemble optimizations at fine-scale grid boxes around the  
73 globe is prohibitively computationally intensive.

74 At the expense of sacrificing the full capability of a physics-based model, we can take advantage  
75 of a statistical approach to predict  $\text{PO}_3$  using several observable variables with improved computational  
76 efficiency. Chatfield et al. (2010) made an early effort to parameterize the gross production of ozone via  
77  $\text{NO}+\text{HO}_2$  through a multivariable power law function that depended on formaldehyde (HCHO), nitrogen  
78 dioxide ( $\text{NO}_2$ ), UV photolysis rates, and ambient temperature. Their model successfully reproduced over  
79 60% of the variance observed in the ozone gross production rates. Souri et al. (2023a) introduced a bilinear  
80 equation based on  $\text{HCHO} \times \text{NO}_2$  and  $\text{HCHO}/\text{NO}_2$ , which explained more than 80% of the variance in  
81 simulated  $\text{PO}_3$ . Building on these findings, Souri et al. (2025) developed a regularized piece-wise linear  
82 regression to parameterize  $\text{PO}_3$  using retrospective aircraft observations and a set of variables, including  
83  $\text{HCHO}/\text{NO}_2$ , HCHO,  $\text{NO}_2$ ,  $j\text{O}^1\text{D}$  (photolysis frequency for  $\text{O}^1\text{D}+h\nu$ ), and  $j\text{NO}_2$  (photolysis frequency for  
84  $\text{NO}_2+h\nu$ ). Their algorithm successfully reproduced over 90% of the variance in observationally-constrained  
85  $\text{PO}_3$  with minimal biases across moderately to extremely polluted regions.

86 These parameterizations present a unique opportunity to globally map  $\text{PO}_3$ , as their primary inputs  
87 can be largely constrained by well-characterized satellite retrievals with extensive horizontal coverage  
88 (Gonzalez Abad et al. 2019). For this reason, Souri et al. (2025), compiled various satellite observations  
89 including TROPOspheric Monitoring Instrument (TROPOMI) surface albedo, HCHO, and  $\text{NO}_2$  columns  
90 in conjunction with pre-computed model fields to populate the inputs to their parametrization, allowing  
91 them to generate the first-ever maps of  $\text{PO}_3$  worldwide. Because their algorithm had an explicit

92 mathematical form, they were also able to break down  $\text{PO}_3$  into  $\text{HCHO}$  and  $\text{NO}_2$  contributions, providing  
93 much more detailed spatial information about ozone sensitivity maps compared to binary information (i.e.,  
94  $\text{NO}_x$ -sensitive or  $\text{VOC}$ -sensitive) made from  $\text{HCHO}$  to  $\text{NO}_2$  ratios (known as formaldehyde to nitrogen  
95 dioxide ratios – FNR) (Martin et al., 2004; Duncan et al., 2010; Choi et al., 2012; Choi and Souri, 2015a,  
96 b; Jin et al., 2017; Schroeder et al., 2017; Souri et al., 2017; Jeon et al., 2018; Tao et al., 2022; Jonhson et  
97 al., 2024). However, FNR was a central component of their algorithm to transform the non-linear ozone  
98 chemistry into several linear segments (i.e., a piecewise regression).

99 The inclusion of FNR in Souri et al. (2025) introduces several complications, such as i) the  
100 amplification of unresolved systematic and random errors in satellite retrievals associated with  $\text{PO}_3$   
101 estimates, and ii) discounting the dependency of  $\text{PO}_3$  sensitivity to  $\text{HCHO}$  and  $\text{NO}_2$  concentrations as  
102 function of available light and water vapor. In fact, FNR does not provide useful information about ozone  
103 chemistry in less photochemically active environments, such as early morning or late afternoon conditions  
104 (known as light-limited or radical-limited conditions). Although the parametrization of  $\text{PO}_3$  crafted in Souri  
105 et al. (2025) relied on photolysis rates, the sensitivity of  $\text{PO}_3$  to  $\text{NO}_2$  (a proxy for reactive nitrogen) and  
106  $\text{HCHO}$  (a proxy for  $\text{VOC}$  reactivity) did not directly depend on photolysis rates.

107 The overarching goal of producing ozone chemistry sensitivity maps is to inform regulatory  
108 agencies about the impact of emission reductions on locally produced ozone. Unlike conventional FNR-  
109 based binary maps, these maps must quantify the magnitude of sensitivity rather than merely indicating its  
110 direction. This quantitative approach is essential because both the sign and magnitude of sensitivities are  
111 crucial for understanding the impact of emission changes. While detailed sensitivity maps can be derived  
112 from chemical transport models by perturbing underlying emissions, the lack of observational constraints  
113 on these models can introduce significant biases. Souri et al. (2025) attempted to address this limitation by  
114 providing magnitude-dependent sensitivity maps of  $\text{PO}_3$  to  $\text{NO}_2$  and  $\text{HCHO}$  using piecewise linear  
115 regression. However, their approach yielded derivatives of  $\text{PO}_3$  with respect to  $\text{NO}_2$  and  $\text{HCHO}$  that  
116 remained invariant with changes in light and humidity conditions. This limitation is problematic because  
117 reduced light conditions are known to substantially dampen the sensitivity of  $\text{PO}_3$  to  $\text{NO}_x$  and  $\text{VOCs}$ , even  
118 under identical emission rates. The current work is therefore motivated by the need to capture the complex,  
119 multidimensional dependencies of  $\text{PO}_3$  on ozone precursors, light intensity, and humidity using a more  
120 flexible data-driven approach through a machine learning algorithm without the need for segregation or  
121 linearization. While these maps will not replace process-based chemical transport model experiments, they  
122 can efficiently provide first-order assessments to: (i) strategize improved modeling experiments, (ii) gauge  
123 the added value of satellites on predictions of  $\text{PO}_3$ , and (iii) guide the design of sub-orbital missions in  
124 regions with poorly documented elevated  $\text{PO}_3$ .

125 The new product of  $\text{PO}_3$  along with spatially varying ozone sensitivity maps using bias-corrected  
126 OMI and TROPOMI retrievals are generated globally for 2005-2023. We will document the advantages of  
127 this algorithm over the older one and how the new results can bring fresh insights into  $\text{PO}_3$  behavior across  
128 various seasons, locations, and global trends.

## 129 2. Data

### 130 2.1. Satellite Retrievals

#### 131 2.1.1. TROPOMI HCHO and $\text{NO}_2$

132 We use daily level-2 (L2) products of TROPOMI (v2.4-v2.5) tropospheric  $\text{NO}_2$  and total  $\text{HCHO}$   
133 columns (v2.4-v2.6) obtained from UV-Vis radiances ( $\sim 328$ -496 nm) onboard the European Space  
134 Agency's (ESA's) Sentinel Precursor (S5P) spacecraft with an equatorial overpass time of  $\sim 1330$  local  
135 standard time (LST) (Veefkind et al., 2012; van Geffen et al. 2022; De Smedt et al. 2021). These products  
136 offer near-daily global coverage of  $\text{NO}_2$  and  $\text{HCHO}$  columns at a horizontal resolution of 7.2 km (reduced

137 to 5.6 km after August 2019) by 3.6 km at nadir, extending to approximately 14 km at the edges of the  
138 scanline, with a swath width of 2600 km. The data products used in this study span from May 2018 to the  
139 end of 2023. The retrieval process follows a two-step framework: first, a differential spectral fitting  
140 algorithm is used to determine the number of integrated molecules along the slant light path, and second,  
141 air mass factor calculations are done based on simulated gas absorber profiles and radiative transfer model  
142 calculations to convert slant columns into vertical ones.

143 Both products have been thoroughly vetted against ground-based remote sensing retrievals,  
144 including the multi-axis differential optical absorption spectrometer (MAX-DOAS) (De Smedt et al., 2021;  
145 Verhoelst et al., 2021; van Geffen et al. 2022; Souri et al., 2025) and Fourier transform infrared spectroscopy  
146 (FTIR) (Vigouroux et al., 2020; Souri et al., 2025), showing a general tendency towards underestimation in  
147 polluted regions. We include in our study only pixels with a quality flag ( $q\_value$ ) exceeding 0.5 and 0.75  
148 for HCHO and NO<sub>2</sub> products, respectively. The quality flag encapsulates errors coming from clouds, snow,  
149 surface refractivity, and algorithm performance. The selected values are based on the user manual  
150 recommendation. The daily HCHO and NO<sub>2</sub> columns, along with the retrieval errors, are mapped onto a  
151 0.1°×0.1° global grid using a mass-conserved bilinear interpolation approach described in Souri et al.  
152 (2024).

### 153 2.1.2. OMI HCHO and NO<sub>2</sub>

154 We use the Quality Assurance for the Essential Climate Variables (QA4ECV) NO<sub>2</sub> daily Level 2  
155 product (Boersma et al., 2018) which is based on global radiances captured by the Ozone Monitoring  
156 Instrument (OMI) sensor aboard NASA's Aura spacecraft. This product is retrieved with a similar overpass  
157 time as TROPOMI. The horizontal resolution of the product ranges from 13×24 km<sup>2</sup> at nadir to 165×13  
158 km<sup>2</sup> at the edge of the scanline. It relies on OMI Collection 3 radiance data. Since 2008, OMI has faced  
159 significant anomalies resulting in the loss of reliable data in areas of its detector, a situation referred to as  
160 the "row anomaly." This has led to inconsistent spatial resolution and global coverage throughout its  
161 operational phase. However, the unaffected pixels have demonstrated a high level of stability over the past  
162 two decades, making this product suitable for long-term trend analysis. Detailed description of the retrieval  
163 algorithm, along with validation against ground remote sensing data, can be found in Boersma et al. (2018),  
164 Compernolle et al. (2020), and Pinardi et al. (2020). We include good quality pixels based on an effective  
165 cloud fraction below 50%, a quality processing flag parameter equal to zero, and exclusion of snowy  
166 regions. Additionally, we discard the last two rows of the detector because of their poor horizontal  
167 resolution. We use the OMI NO<sub>2</sub> product for the period from 2005 until the end of 2019.

168 We also use the OMI Smithsonian astrophysical observatory (SAO) daily HCHO Level 2 product  
169 from the same sensor, which is generated using a newly developed algorithm and Collection 4 OMI  
170 radiances (Ayazpour et al. 2025; Nowlan et al., 2023). This improved algorithm enhances the radiance  
171 information content used to retrieved HCHO columns, significantly reducing noise in the slant column fit.  
172 The stability of this product in extracting new information related to long-term global trends of HCHO has  
173 been well demonstrated in recent studies (Souri et al., 2024; Anderson et al., 2024). We include only good  
174 data following the quality flag provided with the dataset along with effective cloud fraction below 40%.  
175 Both OMI products are mapped onto a global grid with a resolution of 0.25°×0.25° using the same algorithm  
176 used for TROPOMI daily.

### 177 2.1.3. *Bias correction using ground-based remote sensing data*

178 In order to remove large biases in both TROPOMI and OMI products, we bias correct their columns  
179 using the offset (additive term) and slope (multiplicative term) determined from a linear fit to paired MAX-  
180 DOAS/FTIR and these datasets, as described by Souri et al. (2025). The rationale for defining retrieval  
181 biases as a function of magnitude is to enhance correction factor generalizability across seasons and  
182 locations. We take advantage of three studies characterizing the bias correction factors, listed in Table 1.

183 The application of these correction factors yields consistency across OMI and TROPOMI NO<sub>2</sub> and HCHO  
 184 columns within 10% (Section 4.4.4)

185 **Table 1.** The slopes and offsets derived from various validation studies used to bias correct the  
 186 satellite retrievals employed in the parameterization of PO<sub>3</sub>.

Product	Slope	Offset	Benchmark	Time period of validation	Reference
TROPOMI NO <sub>2</sub>	0.66	$0.32 \times 10^{15}$ molec/cm <sup>2</sup>	Global MAX-DOAS observations	2018-2023	Souri et al., (2025)
TROPOMI HCHO	0.59	$0.90 \times 10^{15}$ molec/cm <sup>2</sup>	Global observations	FTIR 2018-2023	Souri et al., (2025)
OMI NO <sub>2</sub>	0.83	$0.26 \times 10^{15}$ molec/cm <sup>2</sup>	Global MAX-DOAS observations	Varies for each station spanning from 2010-2018	Pinardi et al., (2020)
OMI HCHO	0.79	$0.82 \times 10^{15}$ molec/cm <sup>2</sup>	Global observations	FTIR Varies for each station spanning from 2004-2020	Ayazpour et al., (2025)

#### 187 2.1.4. *Surface albedo*

188 To estimate near-surface photolysis rates of jO<sup>1</sup>D (O<sub>3</sub>+hv, <350 nm) and jNO<sub>2</sub> (NO<sub>2</sub>+hv, ~400-500  
 189 nm) used in the parametrization of PO<sub>3</sub>, we are required to provide reasonable surface albedo estimates  
 190 (Section 2.4). We use a monthly Directionally Dependent Lambertian-Equivalent reflectivity (DLER)  
 191 climatology derived from TROPOMI radiances at the spatial resolution of 0.125°×0.125°; the product is in  
 192 good agreement with the MODIS BRDF product (Tilstra et al., 2024). This climatology has two sets of  
 193 values for both shortwave (328 nm) and longwave UV (463 nm) that are used separately for calculating  
 194 jO<sup>1</sup>D and jNO<sub>2</sub>, respectively. We use only the isotropic part of the DLER product (named *minimum\_LER*),  
 195 which is added to an offset coefficient provided with the dataset.

#### 196 2.2. *Aircraft Measurements*

197 The use of aircraft observations is twofold: first, they provide a vast number of measured  
 198 geophysical variables suitable to simulate our observationally-constrained PO<sub>3</sub> training dataset (Section  
 199 3.1); second, they enable a rigorous validation of column-to-planetary boundary layer (PBL) conversion  
 200 factors derived from a chemical transport model (Appendix B). We use the dataset compiled by Souri et al.  
 201 (2025), who curated various aircraft campaigns measuring photolysis rates, meteorological variables, and  
 202 atmospheric composition from varying atmospheric conditions, including urban/suburban settings  
 203 (DISCOVER-AQs, and KORUS-AQ), high-vegetated regions (SENEX), and remote areas (INTEX-B and  
 204 AToms). The sampling frequency varies from 10-sec to 30-sec. More detailed information regarding the  
 205 choice of instrument, gap filling, and data exclusion can be found in Souri et al. (2025).

#### 206 2.3. *MINDS simulations*

207 We use a global chemical transport model simulation designed to support trace gas retrievals. The  
 208 simulation, called Multi-Decadal Nitrogen Dioxide and Derived Products from Satellites (MINDS) (Fisher  
 209 et al., 2024), was generated using the Goddard Earth Observing System (GEOS) Earth system model

(Molod et al., 2015; Nielsen et al., 2017) equipped with the full chemistry Global Modeling Initiative (GMI) mechanism (Duncan et al., 2007; Strahan et al., 2007) and coupled with the Goddard Chemistry Aerosol Radiation and Transport (GOCART) aerosol module (Chin et al., 2002). The rapid radiative transfer model, which was designed for global climate models (GCMs) and is known as the Radiative Transfer Module for GCM (RTTMG), calculates the longwave and shortwave radiation influenced by aerosols simulated by GOCART, enabling the incorporation of the direct effects of aerosols on meteorological conditions (Nielsen et al., 2017). Meteorology is resolved using GEOS with several prognostic inputs, including water vapor, being constrained by MERRA-2 reanalysis using “replay” mode at 3-hourly basis (Orbe et al., 2017). The model is setup at c360 grid ( $0.25^\circ \times 0.25^\circ$ ) and covers the period of 1993 until the end of 2023. The model follows 72 hybrid sigma values ranging from the surface to 0.01 hPa.

Lightning production of NO is parametrized based on the simulated convection. The model uses the Monitoring Atmospheric Chemistry and Climate and CityZen (MACCity) inventory (Granier et al., 2011) of anthropogenic emissions downscaled to  $0.1^\circ \times 0.1^\circ$  using the Emissions Database for Global Atmospheric Research version 4.2 (EDGAR 4.2). These anthropogenic emissions change by year and month. Biomass burning emissions rely on the Fire Energetics and Emissions Research (FEER) dataset (Ichoku and Ellison, 2014). Biogenic emissions are modeled interactively by the Model of Emissions of Gases and Aerosols from Nature (MEGAN) v2.1 (Guenther et al. 2012). It is known that isoprene emissions in MEGANv2.1 are largely overestimated (Bauwens et al., 2016; Souri et al., 2020b), therefore they are scaled down by a factor of two.

#### 2.4. *TUV NCAR Photolysis Rates Look-up Table*

To estimate  $j\text{NO}_2$  and  $j\text{O}^1\text{D}$ , we refer to a detailed look-up table provided by the Framework for 0-D Atmospheric Modeling (F0AM) model (Wolfe et al. 2016). This table is developed for clear-sky conditions based on over 20,064 solar spectra calculations. The data encompasses a broad spectrum of solar zenith angles (SZA) from  $0^\circ$  to  $90^\circ$  in  $5^\circ$  increments, altitudes ranging from 0 to 15 km in 1 km steps, overhead total ozone columns from 100 to 600 DU in increments of 50 DU, and surface UV albedo values from 0 to 1 in 0.2 increments. These calculations were carried out using NCAR’s Tropospheric Ultraviolet and Visible radiation model (TUV v5.2), along with cross sections and quantum yields from IUPAC and JPL (Wolfe et al., 2016). Information on SZA and surface elevation is obtained from the L2 TROPOMI/OMI granule data. Surface albedo is based on the TROPOMI DLER climatology (Section 2.1.4). The overhead total ozone columns are derived from MINDS simulations (Section 2.3). For any values that fall between the entries in the tables, we apply a linear interpolation method.

#### 2.5. *Empirical $\text{PO}_3$ estimates using LASSO*

We will compare our new product (Section 3.2) to an empirical method developed by Souri et al. (2025), who took advantage of simulated  $\text{PO}_3$  data constrained by aircraft measurements to parameterize  $\text{PO}_3$  using four geophysical variables:  $\text{NO}_2$ ,  $\text{HCHO}$ ,  $j\text{NO}_2$ , and  $j\text{O}^1\text{D}$ . Their algorithm used a piecewise L1-regularized linear regression model known as Least Absolute Shrinkage and Selection Operator (LASSO). Since the algorithm was based on a linear model which was ill-suited for the non-linear ozone chemistry, it was necessary to linearize the parameterization using various thresholds for FNRs. Despite the method’s simplicity, Souri et al. (2025) were able to reproduce approximately 88% of the variance with low biases (less than 20%) in observationally-constrained  $\text{PO}_3$ . Using the empirical method, they generated the first maps of  $\text{PO}_3$  by combining bias-corrected TROPOMI  $\text{HCHO}$  and  $\text{NO}_2$  columns, simulated photolysis rates, and a global transport model designed for the conversion from column measurements to the PBL.

To isolate the performance of the  $\text{PO}_3$  estimator used in Souri et al. (2025) in comparison to the proposed algorithm in this study, we will ensure that the input variables, including the mixing ratios of  $\text{HCHO}$  and  $\text{NO}_2$  within the PBL as well as the photolysis rates, remain identical for both the empirical product and our new algorithm. Hereafter, we will refer to this empirical product as “ $\text{PO}_3\text{LASSO}$ ”.

256 3. Methodology

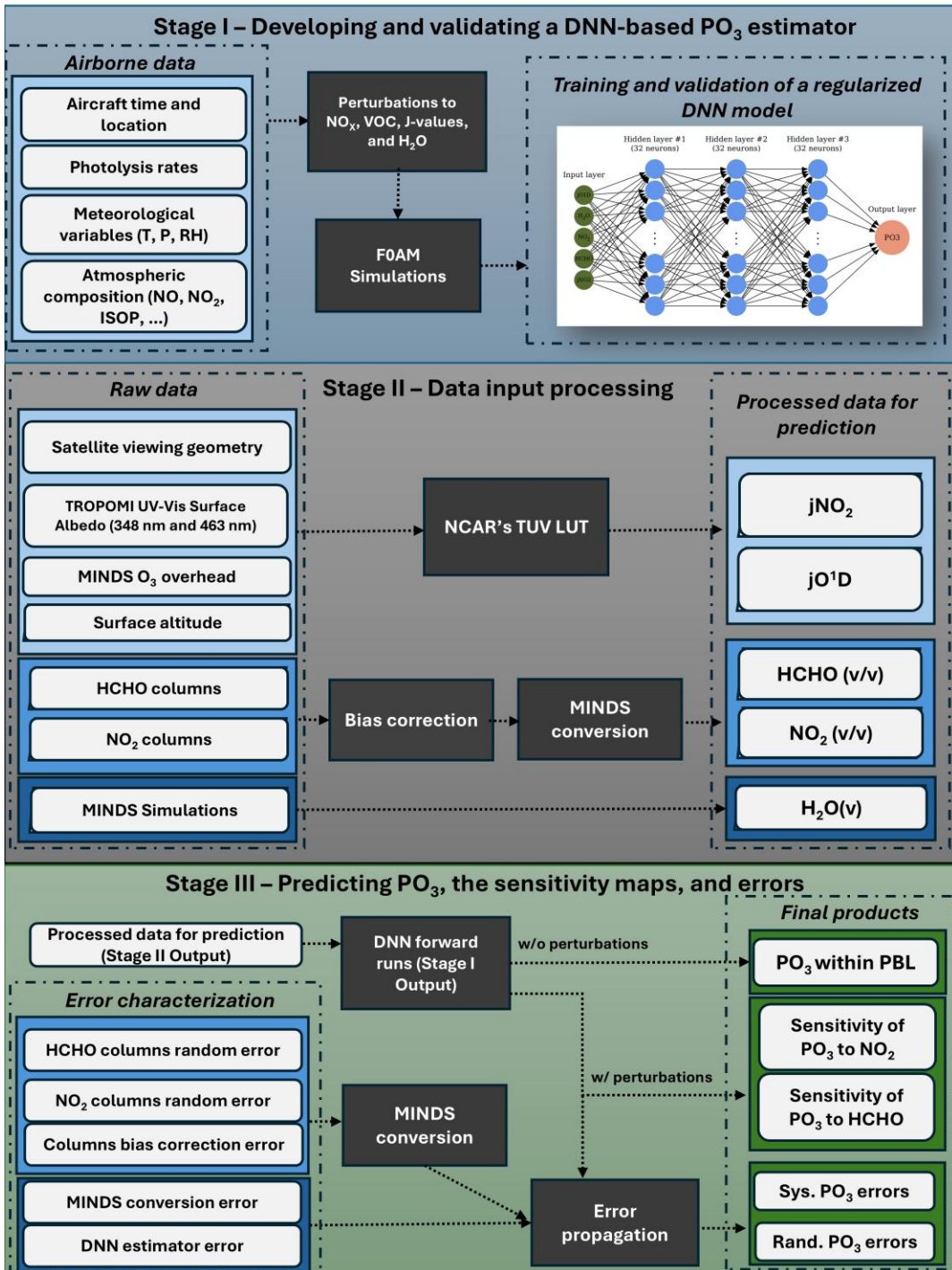
257 Figure 1 illustrates the three-stage process of our newly developed algorithm to operationally  
258 produce long-term maps of  $\text{PO}_3$  within the PBL along with the sensitivity and error maps. The product is  
259 called “ $\text{PO}_3\text{DNN}$ ”.

260 *Stage I*—This stage serves as the foundation for the product, focusing on parameterizing  $\text{PO}_3$  using  
261 a regularized Deep Neural Network (DNN). The training dataset, detailed in Section 3.1, is derived from  
262 an observationally-constrained F0AM box model that provides simulated  $\text{PO}_3$  along with various  
263 atmospheric quantities directly or indirectly constrained by aircraft measurements. The decision to make  
264 use of aircraft data is based on two main factors: i) they capture real-world atmospheric conditions across  
265 diverse parts of the atmosphere and various geographic regions, and ii) the significant fluctuations inherent  
266 in the data rigorously test the DNN’s capability to generalize (i.e., to fit the model through the data rather  
267 than merely to the data). However, a notable limitation of aircraft data is its restriction to specific  
268 atmospheric conditions. To address this, we have expanded the training dataset by perturbing the inputs to  
269 the F0AM model (Section 3.1), resulting in a synthetic dataset. This expanded training dataset is then used  
270 for validation, testing, and calibration of the DNN algorithm.

271 *Stage II*—The objective of this stage is to prepare spatiotemporal geophysical variables necessary  
272 for the prediction of  $\text{PO}_3$  (done in Stage III). We need five parameters on a global scale with daily frequency:  
273  $\text{jNO}_2$ ,  $\text{jO}^1\text{D}$ ,  $\text{HCHO}$ ,  $\text{NO}_2$ , and  $\text{H}_2\text{O}(\text{v})$ . To generate global daily maps of near-surface photolysis rates, we  
274 use the NCAR’s look-up table as detailed in Section 2.4; this table relies on SZA, which varies with time  
275 and location, as well as surface UV-Vis albedo, ozone overhead columns, and surface altitudes. Both SZA  
276 and surface altitude are provided as auxiliary fields in the satellite L2 products. Ozone overhead columns  
277 are from MINDS. For surface UV-Vis albedo, we use two different wavelengths based on TROPOMI’s  
278 climatology (Section 2.1.4). These calculations assume clear sky conditions, which are somewhat achieved  
279 by the effective cloud fraction thresholds derived from both the OMI and TROPOMI products. Our  
280 algorithm uses  $\text{HCHO}$  and  $\text{NO}_2$  columns obtained from OMI or TROPOMI, which are bias-corrected  
281 against ground remote sensing data. These measurements are then transformed into the mixing ratios in the  
282 PBL region using the vertical distribution of  $\text{HCHO}$  and  $\text{NO}_2$  profiles simulated by MINDS. The final  
283 variable is the average number of water vapor ( $\text{H}_2\text{O}(\text{v})$ ) molecules per cubic meters in the PBL region at  
284 the satellite overpass time, which is obtained directly from the MINDS simulation. It is important to note  
285 that the MINDS simulation is based on constraints from MERRA-2 reanalysis, underscoring that the  $\text{H}_2\text{O}(\text{v})$   
286 simulations are constrained by many observations.

287 *Stage III*—In the final stage, we predict  $\text{PO}_3$ , generate sensitivity maps, and provide both systematic  
288 and random errors associated with these estimates. To create  $\text{PO}_3$  maps, we input the five parameters from  
289 Stage II into the DNN model developed in Stage I. To generate the sensitivity maps of  $\text{PO}_3$  in relation to  
290  $\text{NO}_2$  and  $\text{HCHO}$ , we apply perturbations to  $\text{NO}_2$  and  $\text{HCHO}$  based on the methodology described in Section  
291 3.3. These perturbations also serve another purpose which is to propagate the errors associated with the  
292 retrievals of  $\text{HCHO}$  and  $\text{NO}_2$ , as well as their corresponding conversion factors from MINDS into the final  
293 product. A comprehensive explanation of the error budget and characterization can be found in Section 3.4.

294 While we perform Stage I only once to establish a  $\text{PO}_3$  estimator, we need to run Stage II and III  
295 for any desired location/time or spatial resolution. The need to operationally run these two stages has  
296 motivated us to create an open-source and object-oriented Python package called *ozonerates* v1.0 (Souri  
297 and Gonzalez Abad, 2025), which is capable of running all steps while leveraging parallel computation.



298

299 **Figure 1.** Processing stages developed to operationally generate  $\text{PO}_3$  and sensitivity maps along with daily  
300 frequency errors on a global scale. Stage I aims to establish a regularized DNN model based on synthetic  
301 and real-world aircraft measurements. Stage II prepares the necessary satellite-based input features used for  
302  $\text{PO}_3$  prediction in Stage III. Stage III feeds the DNN model with Stage II values and some statistical error  
303 analysis to generate the final product.

304    **3.1. Training dataset generation using F0AM box model**

305    To establish a relationship between several geophysical variables related to  $\text{PO}_3$ , we use F0AM  
 306    version 4 box model (Wolfe et al., 2016). This model is capable of simulating detailed chemical kinetics  
 307    based on user inputs regarding meteorological variables, atmospheric compositions, and photolysis rates.  
 308    F0AM uses a solver for ordinary differential equations (ODEs) designed for stiff systems, which allows it  
 309    to determine the chemical evolution of all species included in the selected chemical mechanism. We adhere  
 310    to previous configurations that apply the Carbon Bond 6 (CB06, r2) chemical mechanism within F0AM  
 311    (Souri et al., 2020a; Souri et al., 2023a; Souri et al., 2025). The model is constrained by data collected  
 312    during aircraft campaigns, including meteorological data, photolysis rates, and various trace gas  
 313    concentrations. Additional details regarding the selection of instruments, bias corrections for photolysis,  
 314    choices of dilution factors, and other configurations can be found in Souri et al. (2025). We incorporate data  
 315    from seven aircraft campaigns, including DISCOVER-AQ (Texas, Washington D.C., Colorado), KORUS-  
 316    AQ, ATOMs, INTEX-B, and SENEX, to further constrain the model. Souri et al. (2025) demonstrated that  
 317    this setup effectively reproduces several unconstrained yet measured compounds, such as  $\text{HCHO}$ ,  $\text{HO}_2$ ,  
 318     $\text{OH}$ , and  $\text{PAN}$ ; moreover, the performance of the model was on par with other studies (e.g., Brune et al.,  
 319    2020; Brune et al., 2022; Miller and Brune, 2022), indicating that it is a suitable model setup for  
 320    understanding local ozone chemistry. This model-derived dataset consists of ~134k points.

321    A limitation to the training dataset prepared by Souri et al. (2025) originates from the fact that only  
 322    a subset of atmospheric conditions could be observed by the suborbital missions. A remedy for this  
 323    limitation is to synthetically regenerate data by systematically perturbing several of the inputs used in the  
 324    F0AM model. As a result, we apply a scaling factor, ranging from 0.1 up to 10 in 12 evenly-spaced steps,  
 325    separately to  $\text{NO}_x$ , VOCs,  $\text{H}_2\text{O}(\text{v})$ , and photolysis rates. This expands the dataset to ~6.4 million datapoints,  
 326    covering a much wider range of atmospheric states.

327    Once the simulations are done, we determine simulated  $\text{PO}_3$  by:

$$PO_3 = FO_3 - LO_3 \quad (1)$$

328    where  $LO_3$  is all possible chemical loss pathways of ozone (negative stoichiometric multiplier matrix) and  
 329     $FO_3$  is all possible chemical pathways producing ozone molecules (positive stoichiometric multiplier  
 330    matrix). This equation is also known as ozone tendency. This definition simplifies intercomparison with  
 331    estimates derived from different chemical mechanisms by eliminating the requirement to explicitly match  
 332    individual production and loss terms, which often exhibit inconsistencies across mechanisms, especially in  
 333    their treatment of peroxy radicals. The calculation of  $\text{PO}_3$  is under a steady-state assumption.

334    **3.2. DNN architecture and configuration**

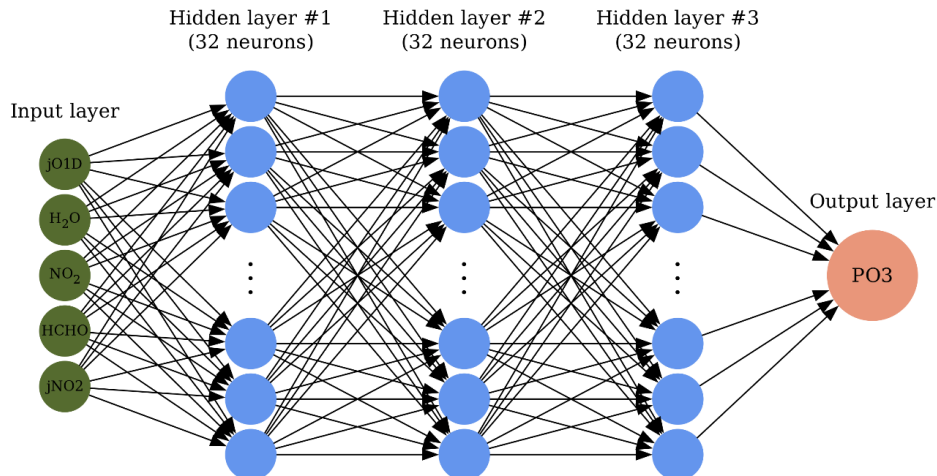
335    The overall architecture of the DNN model is portrayed in Figure 2. The design consists of three  
 336    fully-connected hidden layers each having 32 neurons. The neurons are equipped with rectified linear unit  
 337    (ReLU) activation functions. The training dataset (~6.4 millions) is split into 20% test, 24% validation, and  
 338    56% training. Training inputs to the parametrization consists of  $\text{HCHO}$ ,  $\text{NO}_2$ ,  $\text{jO}^1\text{D}$ ,  $\text{jNO}_2$ , and  $\text{H}_2\text{O}(\text{v})$ .  
 339    Prior to the training, we normalize them, such that each feature ( $x$ ) is rescaled according to  $x' = \frac{x-\mu}{\sigma}x$ ,  
 340    where  $\mu$  and  $\sigma$  represent the mean and standard deviation of the feature, respectively, ensuring a mean of  
 341    zero and a variance of one. The optimization (training) of the DNN follows the backpropagation rule armed  
 342    with Adaptive Moment Estimation (ADAM) optimizer which is known to perform well with noisy data  
 343    (Kingma and Ba, 2014). The initial learning rate is set to  $10^{-5}$ . We use 500 epochs. The loss function ( $L$ ) of  
 344    the optimization problem is:

$$L = \frac{1}{2} \sum_{k=1}^N (y_k - o_k)^2 + \lambda \sum_{i=1}^p w_i^2 \quad (2)$$

345 where the first term on the right side represents the mean squares error (MSE) of the prediction derived  
 346 from difference between the target  $\text{PO}_3$  ( $y$ ) and the predicted  $\text{PO}_3$  ( $o$ ).  $N$  represents the number of training  
 347 datapoints. The second term is L2-regularization with a factor of  $\lambda$  to reduce the squares of  $p$  number of  
 348 neuron weights ( $w$ ).

349 An important aspect of this optimization is the use of L2 regularization, which effectively helped  
 350 us determine the optimal number of hidden layers and neurons. L2 regularization penalizes the cost function  
 351 if an illusion of high prediction accuracy (the first term) is achieved with excessive variance in the solution  
 352 (weights). Failing to balance the prediction error and the solution variance can lead to overfitting, which  
 353 harms model performance in two ways: i) it results in erroneous predictions for atmospheric conditions that  
 354 fall outside the training dataset; ii) it diminishes the physical interpretability of the statistical model because  
 355 of large fluctuations in the weights, a common issue in regression models known as collinearity. When we  
 356 used too many neurons or layers, the regularization penalized the weights, causing a substantial proportion  
 357 to approach zero (not shown), indicating that those neurons were unnecessary. However, incorporating  
 358 regularization does have some drawbacks: i) it requires a smaller initial learning rate (set to  $10^{-5}$ ) to avoid  
 359 falling into local minima, which demands more computational resources; and ii) the regularization factor  
 360 also needs to be optimized. We find that a value of  $\lambda = 10^{-5}$  provides the best results among the set of values  
 361 [ $10^{-4}$ ,  $10^{-5}$ , and  $10^{-6}$ ], based on the symmetry in the statistical distributions of the test residuals, MSE, and  
 362 the overall level of physical interpretability observed in the sensitivity tests.

363 The implementation of the DNN model is done using the open-source *TensorFlow* application  
 364 programming interface (API) package in *Python* (Abadi et al., 2016). To thoroughly validate the  
 365 performance of this model from various angles we i) compare the DNN prediction with the test data using  
 366 various standard metrics, ii) investigate the evolution of the loss function derived from both the training set  
 367 and the validation one over epochs, iii) study the physical explanation of the response of  $\text{PO}_3$  to  $\text{NO}_2$  and  
 368  $\text{HCHO}$ , water vapor, and photolysis rates, and iv) finally compare the DNN results to  $\text{PO}_3$ LASSO. We will  
 369 use a number of statistical metrics, including the coefficient of the determination ( $R^2$ ), mean bias, mean  
 370 square error, mean absolute error, and root mean square error (RMSE), to carry out the quantitative  
 371 assessment (Section 4.1).



372  
 373 **Figure 2.** The architecture of the DNN model. The model contains three hidden layers with 32 neurons  
 374 each.

375 **3.3. Sensitivity calculations**

376 To elucidate the response of  $\text{PO}_3$  to its inputs, we calculate the semi-normalized sensitivities  
 377 through the finite difference method:

$$SP03_i = \frac{[PO3]_i^{110\%} - [PO3]_i^{90\%}}{0.2} \quad (3)$$

378 where  $[PO3]_i^{110\%}$  and  $[PO3]_i^{90\%}$  are  $PO_3$  from perturbing input parameters ( $i=1$  for  $NO_2$ , and  $i=2$  for  
379  $HCHO$ ) by 1.1 and 0.9 scaling factors. A mathematical proof showing that these sensitivity calculations  
380 are equivalent to the directional derivative is provided in Appendix A.

381 **3.4. Error budget and characterization**

382 Since the  $PO_3$ DNN integrates atmospheric models, satellite trace gas retrievals, ground remote  
383 sensing, and a machine learning approach, it contains various sources of errors, some of which will be  
384 formulated in this section. Spatially and temporally averaging satellite-based products is a common practice  
385 to reduce noise and fill gaps; therefore, we attempt to separate systematic errors (irreducible by averaging)  
386 from random ones (reducible by averaging). We assign the total  $PO_3$  within PBL region error ( $e_{total}$ ) based  
387 on the following equation:

$$e_{total} = \sqrt{e_{syst}^2 + e_{rand}^2} \quad (4)$$

388 where  $e_{syst}$  and  $e_{rand}$  are systematic and random errors associated with  $PO_3$  estimates. Systematic errors  
389 account for the errors associated with the bias correction of OMI and TROPOMI against ground remote  
390 sensing retrievals ( $e_{HCHO\_bias\_c}$  and  $e_{NO2\_bias\_c}$ ), the model-based conversion of columns to the PBL mixing  
391 ratios ( $e_{HCHO\_conversion}$ ,  $e_{NO2\_conversion}$ ), and the DNN estimator error ( $e_{DNN}$ ), and are given by:

$$392 e_{syst} = \sqrt{e_{HCHO\_bias\_c}^2 + e_{NO2\_bias\_c}^2 + e_{HCHO\_conversion}^2 + e_{NO2\_conversion}^2 + e_{DNN}^2} \quad (5)$$

$$393 e_{HCHO\_bias\_c}^2 = \left( \frac{\partial PO_3}{\partial HCHO} \cdot \gamma \cdot e_{bc-HCHO} \right)^2 \quad (6)$$

$$394 e_{NO2\_bias\_c}^2 = \left( \frac{\partial PO_3}{\partial NO_2} \cdot \gamma \cdot e_{bc-NO_2} \right)^2 \quad (7)$$

$$395 e_{HCHO\_conversion}^2 = \left( \frac{\partial PO_3}{\partial HCHO} \cdot VCD_{HCHO} \cdot e_{conv-HCHO} \right)^2 \quad (8)$$

$$396 e_{NO2\_conversion}^2 = \left( \frac{\partial PO_3}{\partial NO_2} \cdot VCD_{NO_2} \cdot e_{conv-NO_2} \right)^2 \quad (9)$$

397 where  $\gamma$  is the conversion factor of the satellite total to the PBL columns translation based on MINDS and  
398 the formulation by Souri et al. (2025);  $e_{bc-HCHO}$  and  $e_{bc-NO_2}$ , in column units, are calculated following the  
399 formulation from Souri et al. (2025) who used the errors of slope and offset obtained from the comparison  
400 of satellite VCDs to ground remote sensing benchmarks;  $e_{conv-HCHO}$  and  $e_{conv-NO_2}$  are quantified by validating  
401 the simulated conversion factors compared to those of aircraft vertical spirals (Appendix B). The unit for  
402 these two errors is ppbv per the column unit; accordingly, we multiply these terms to satellite VCDs. The  
403 last term in Eq.5 is a fixed systematic error associated with the DNN estimates which will be quantified  
404 based on the MSE of the DNN prediction. Both  $\frac{\partial PO_3}{\partial HCHO}$  and  $\frac{\partial PO_3}{\partial NO_2}$  are derived from the sensitivity calculations  
405 from Eq.3 divided by the satellite columns. All error terms in Eqs.6-9 are spatially and temporally invariant,  
406 but the derivatives vary from pixel to pixel resulting in spatiotemporally-varying systematic errors.

407 Random errors originate from the uncertainty estimates coming with the TROPOMI and OMI L2  
408 products and are somewhat reducible by averaging, and are given by:

$$e_{rand} = \sqrt{\left( \frac{\partial PO_3}{\partial HCHO} \cdot \gamma \cdot e_{rand-HCHO} \right)^2 + \left( \frac{\partial PO_3}{\partial NO_2} \cdot \gamma \cdot e_{rand-NO_2} \right)^2} \quad (10)$$

409 where  $e_{rand-HCHO}$  and  $e_{rand-NO_2}$  are random retrieval errors. All terms in Eq.10 vary by time and location.

410 Table 2 summarizes the numbers used in the above equations and their origin.

411 **Table 2.** Values used in error calculations.

Error terms	Systematic/Random	Value	Unit	Source
$e_{bc-NO_2}$ and $e_{bc-HCHO}$	Systematic	$0.01 \times VCD + 0.06$	$\times 10^{15}$ molec./cm <sup>2</sup>	Souri et al. (2025)
$e_{conv-HCHO}$ and $e_{conv-NO_2}$	Systematic	0.09	ppbv/( $10^{15}$ molec./cm <sup>2</sup> )	Appendix B
$e_{DNN}$	Systematic	0.88	ppbv/hr	Section 4.1
$e_{rand-NO_2}$ and $e_{rand-HCHO}$	Random	Variable	$\times 10^{15}$ molec./cm <sup>2</sup>	L2 Products

412

413 It is important to acknowledge that the defined total error budget here is only a good guess and  
414 optimistic. Some underlying sources of error, which are difficult to quantify, are not included. For example,  
415 errors related to the training dataset derived from the F0AM model are challenging to assess because of the  
416 lack of PO<sub>3</sub> measurements. We assume other inputs to the PO<sub>3</sub> parametrization, such as the monthly  
417 climatology TROPOMI surface albedo to be error-free. Additionally, all datasets used to estimate PO<sub>3</sub>  
418 contain spatial representation errors (Souri et al. 2022), which are difficult to measure without knowing  
419 their true state of global spatial variability. Moreover, we do not consider correlated errors among HCHO  
420 and NO<sub>2</sub> retrievals. It is worth noting that some of the inputs such as H<sub>2</sub>O(v) and the overhead ozone column  
421 have minimal biases because of MINDS simulations being observationally constrained (Fisher et al., 2024;  
422 Souri et al., 2024).

423 There are also assumptions regarding the equations mentioned earlier. For instance, it is assumed  
424 that the validation of conversion factors can account for all systematic issues related to the vertical  
425 distribution of NO<sub>2</sub> and HCHO in MINDS. Furthermore, we presume that the reported retrieval errors are  
426 mostly random; however, this is not the case (Eskes et al., 2003; Boersma et al. 2018) and distinguishing  
427 between these errors is not straightforward.

428 Another source of uncertainty arises from partially cloudy pixels and aerosols, which can introduce  
429 errors in calculated photolysis rates. While we successfully filtered out cloud cover and strong aerosol  
430 loadings (e.g., from wildfires) using effective cloud fraction thresholds, some aerosol or cloud-  
431 contaminated pixels may pass cloud screening due to low optical depth or height characteristics. Rigorously  
432 quantifying the errors coming from these effects would require running a radiative transfer model with  
433 detailed three-dimensional optical properties of clouds and aerosols on a global scale, particularly critical  
434 for aerosols, which can have complex effects on photolysis rates depending on their absorption and  
435 scattering properties and vertical distribution. Unfortunately, such comprehensive datasets are typically  
436 limited to the narrow swaths of spaceborne lidar observations, which themselves carry substantial  
437 uncertainties (Thorsen and Fu, 2015). While these complications cannot be entirely avoided, particularly  
438 for aerosol effects, users can apply additional quality control measures by filtering pixels using aerosol  
439 optical depth retrievals from TROPOMI, OMI, or other sensors to more rigorously identify contaminated  
440 observations.

441 In case of oversampling of the PO<sub>3</sub> product both temporally and spatially, the total error will be given by:

$$e_{total\_oversampled} = \sqrt{\frac{1}{m} \sum e_{syst}^2 + \frac{1}{m^2} \sum e_{rand}^2} \quad (11)$$

442 where  $m$  is the total number of samples. Eq.11 suggests that the systematic errors are persistent across all  
443 samples and are not reducible by averaging, whereas the random errors become smaller by root square of  
444 samples. In this equation, the assumption is that the root-mean-square of the systematic errors is a good  
445 approximation of the systematic errors in the oversampled data because they are independent of each other.

#### 446 4. Results and Discussion

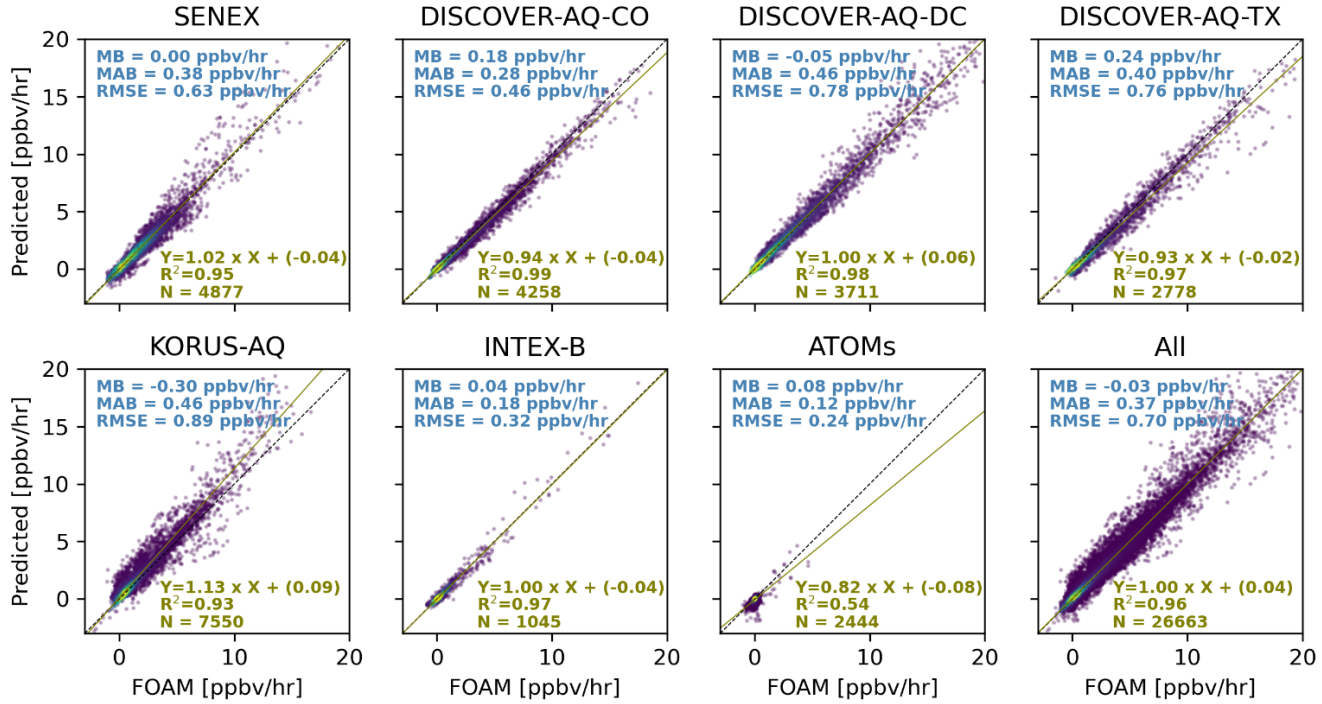
447 In this section, we begin by validating and contrasting  $\text{PO}_3$ DNN against  $\text{PO}_3$ LASSO. Following  
448 that, we use OMI to investigate the spatiotemporal variability of  $\text{PO}_3$  and its sensitivity to photolysis rates,  
449  $\text{HCHO}$ , and  $\text{NO}_2$  globally. We provide an application of data to understand the global long-term trends  $\text{PO}_3$   
450 derived from OMI. Afterward, we offer a comprehensive global view of the  $\text{PO}_3$  estimates algorithm by  
451 integrating data from the TROPOMI compared with that one based on OMI. Finally, we document the total  
452 error budget of the products.

##### 453 4.1. *DNN performance*

454 We investigate the predictive power of the DNN algorithm against both validation and test data for  
455 each air quality campaign or the entire aircraft dataset (Section 2.2). All training datasets described in  
456 Section 3.1 are used in this stage. Except for the early stages of training, both training and validation curves,  
457 explaining the evolution of the prediction against the number of epochs corresponding to the number of  
458 iterations of training the network for one cycle, closely follow each other, indicating that we possibly do  
459 not have overfitting issues (Figure S11). The curves are fairly smooth, resulting from using the ADAM  
460 optimizer with a strictly small learning rate initially. Both curves converge to RMSE below 0.88 ppbv/hr  
461 which we use to assign the error of  $\text{PO}_3$ DNN prediction in Eq.5.

462  $\text{PO}_3$ DNN has promising skill at predicting  $\text{PO}_3$  across various atmospheric conditions. Figure 3  
463 presents a comparison of the predicted  $\text{PO}_3$  values against observationally-constrained F0AM values for  
464 the test data for each suborbital mission. A similar comparison, which includes all data points measured  
465 during each mission, can be found in Figure S12. The primary reason for highlighting the test data is that  
466 they have never been used to fine-tune the DNN parameters. There is a strong correlation between the  
467 predictions and the benchmarks across most campaigns for both the test data points (Figure 3) and the  
468 complete set of aircraft measurements (Figure S12). Notably, the slope for the "All" test dataset is close to  
469 the unity line. The DNN algorithm can reproduce over 96% of the variance in the test data. Similar to the  
470 approach of Souri et al. (2025), we completely exclude each suborbital mission from the training dataset  
471 and use it as an independent benchmark to evaluate the model's performance. The resulting accuracy is  
472 comparable to that achieved when 56% of the data are used for training, indicating that the  $\text{PO}_3$   
473 parameterization has reached a high degree of generalization (Figure S13).

474 The model performs significantly better than  $\text{PO}_3$ LASSO over INTEX-B compared to LASSO (as  
475 shown in Figure 7 in Souri et al., 2025). While the DNN's performance over the ATom campaigns is less  
476 impressive than in other areas, it still represents a considerable improvement over LASSO, which was  
477 unable to reproduce  $\text{PO}_3$  in pristine regions ( $R^2 < 0.05$ ). One key factor contributing to this improvement is  
478 the inclusion of  $\text{H}_2\text{O}(\text{v})$  in the input. Various parameters, including  $\text{HO}_x$ , are known to influence  $\text{PO}_3$  in  
479 remote regions, but these factors were not included in our parametrization. The method does not artificially  
480 inflate results by introducing non-physical relationships in remote regions; the inability of the DNN to fully  
481 explain  $\text{PO}_3$  during AToms suggests that it does not force unrealistic relationships between  $\text{PO}_3$  and the  
482 inputs to completely align with the F0AM results, leaving areas for future improvement in parametrization  
483 over remote regions.



484

485 **Figure 3.** Scatterplots comparing observationally-constrained F0AM model PO<sub>3</sub> and the predictions that  
 486 were based on the DNN for the test data from each air quality campaign. The test data have never been used  
 487 for hyper tuning the algorithm. “All” denotes all test data.

488 **4.2. Advantages of PO<sub>3</sub>DNN over PO<sub>3</sub>LASSO**

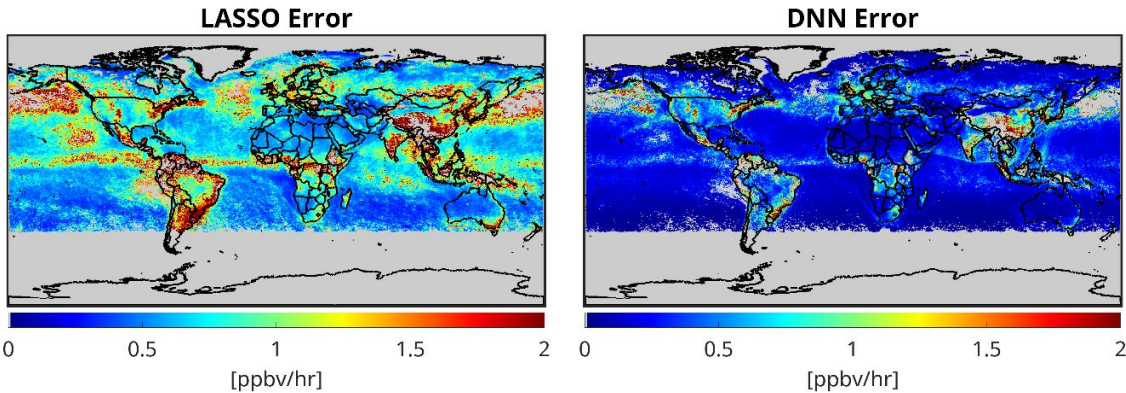
489 There are primarily four major benefits of PO<sub>3</sub>DNN over PO<sub>3</sub>LASSO that make the former parameterization  
 490 a superior algorithm. The discussion of these advantages is as follows:

491 — *Higher predictive power:* PO<sub>3</sub>LASSO predicted PO<sub>3</sub> for all datapoints collected from the suborbital  
 492 missions with a R<sup>2</sup>=0.88, RMSE=1.2 ppbv/hr, and a slope of 0.87 (Souri et al., 2025), whereas PO<sub>3</sub>DNN  
 493 reproduced the exact datapoints (Figure S12) with a R<sup>2</sup>=0.96, RMSE=0.7 ppbv/hr, and a slope of 1.00.  
 494 Furthermore, as shown in Figure 4, PO<sub>3</sub>DNN has a great degree of generalization for datapoints outside  
 495 of the training/validation data points. Consequently, these statistics suggest that DNN is a more  
 496 powerful predictor.

497 — *Better representation of PO<sub>3</sub> over remote regions:* One notable limitation of PO<sub>3</sub>LASSO was its  
 498 inadequate representation of PO<sub>3</sub> in remote regions, such as during the ATOMs or INTEX-B campaigns.  
 499 This led Souri et al. (2025) to entirely mask PO<sub>3</sub> estimates below 1 ppbv/hr. In these remote areas, PO<sub>3</sub>  
 500 is typically influenced by the reactions between ozone and HO<sub>x</sub> in addition to O<sup>1</sup>D and H<sub>2</sub>O. While  
 501 Souri et al. (2025) attempted to incorporate H<sub>2</sub>O into the LASSO parametrization, the algorithm  
 502 assigned a zero coefficient to this parameter because of the use of the L1-regularization term. This term  
 503 typically assigns a zero coefficient for a geophysical variable that is either irrelevant to the target or  
 504 shows strong non-linear relationship with the target. PO<sub>3</sub>LASSO did not factor in H<sub>2</sub>O(v) because  
 505 H<sub>2</sub>O(v) exhibits a non-linear relationship with PO<sub>3</sub> – although the reaction between O<sup>1</sup>D and H<sub>2</sub>O can  
 506 suppress ozone formation through the removal of O<sup>1</sup>D, it produces two molecules of OH regenerating  
 507 ozone in polluted places (Bates and Jacob, 2019). Consequently, the non-linear relationship between  
 508 H<sub>2</sub>O and PO<sub>3</sub> is one that LASSO was unable to capture. While we could have addressed this by dividing  
 509 the training dataset into different humidity levels (i.e., dry and humid), such an approach would have  
 510 resulted in more discretization in the parametrization. Conversely, PO<sub>3</sub>DNN can consider the non-linear

511 relationship between  $\text{H}_2\text{O}$  and  $\text{PO}_3$  without the need for empirical linearization. We observe a significant  
 512 improvement in predicted  $\text{PO}_3$  for both AToms and INTEX-B campaigns compared to Souri et al.  
 513 (2025).

514 — *Diminished satellite error effects*: The reliance of  $\text{PO}_3$ LASSO on FNR increases the contamination of  
 515  $\text{PO}_3$  predictions from satellite random noise. This primarily occurs because satellite errors associated  
 516 with  $\text{HCHO}$  and  $\text{NO}_2$  adversely influence FNR (see Figure 12 in Souri et al. (2023a)), resulting in noise  
 517 in the empirical linearization approach used in  $\text{PO}_3$ LASSO. Even if we assume that all inputs to the  
 518  $\text{PO}_3$ LASSO parameterization, except for FNR, are error-free, the inherent randomness from choosing  
 519 among four different sets of equations segregated by the noisy FNR will still feed noise into the final  
 520 estimate. Although  $\text{PO}_3$ DNN is inevitably influenced by satellite errors because of its dependence on  
 521  $\text{HCHO}$  and  $\text{NO}_2$  columns, it does not exacerbate these errors because it operates independently of FNR.  
 522 To demonstrate this tendency, Figure 4 shows the global  $\text{PO}_3$  random error maps induced by OMI  
 523  $\text{HCHO}$  and  $\text{NO}_2$  retrieval random errors averaged in June 2006. We use identical inputs and errors for  
 524 both algorithms. Figure 4 is evidence of the diminished contamination of satellite random errors in  
 525  $\text{PO}_3$ DNN as compared to  $\text{PO}_3$ LASSO. The error differences tend to be larger over clean areas, because  
 526 FNR random errors are higher when both  $\text{HCHO}$  and  $\text{NO}_2$  levels are small.



527 **Figure 4.** The comparison of the effect of satellite random errors in  $\text{HCHO}$  and  $\text{NO}_2$  on  $\text{PO}_3$  predictions  
 528 based on  $\text{PO}_3$ LASSO and  $\text{PO}_3$ DNN algorithms in June 2006. The data used for generating these maps are  
 529 based on OMI retrievals.  
 530

531 — *Continuity*: It is known that neural networks equipped with three hidden layers can well approximate  
 532 almost any high-dimensional non-linear function (Shen et al., 2021). An important superiority of  
 533  $\text{PO}_3$ DNN over  $\text{PO}_3$ LASSO lies in the strength of the DNN algorithm at approximating high-  
 534 dimensional non-linear relationships between  $\text{PO}_3$  and  $\text{HCHO}$  (a proxy for VOCR),  $\text{NO}_2$  (a proxy for  
 535 reactive nitrogen),  $\text{jNO}_2$  and  $\text{jO}^1\text{D}$  (a proxy for photochemistry), and  $\text{H}_2\text{O}$ . While some of these non-  
 536 linearities were reasonably approximated in  $\text{PO}_3$ LASSO by empirically segregating the chemical  
 537 conditions using FNR, the non-linear ozone photochemistry can go beyond the dependency on VOCs  
 538 and  $\text{NO}_x$  levels. In fact, the relationship between  $\text{PO}_3$  and VOCs and  $\text{NO}_x$  can behave non-linearly  
 539 depending on the available light and water vapor as discussed in Section 4.3. This indicates that  
 540 traditional linear models, such as those using VOCR/ $\text{NO}_x$  (or  $\text{HCHO}/\text{NO}_2$ ) ratios, often fall short in  
 541 capturing this complexity because of the continuous and non-linear nature of these relationships.  
 542

543 **4.3.  $\text{PO}_3$ DNN can capture non-linear  $\text{PO}_3$  chemistry as a function of pollution, light, and  
 544 humidity**

545 To further elaborate on the capability of  $\text{PO}_3$ DNN to reasonably respond to variations in its five  
 546 major parameters in a mathematically continuous fashion, we create six isopleths, each specifically

547 designed to represent a particular atmospheric condition listed in Table 3. These isopleths are based on  
548 perturbing HCHO and NO<sub>2</sub> in PO<sub>3</sub>DNN and are shown in Figure 5.

549 It is immediately apparent that the hyperbolic shape of the PO<sub>3</sub> curve relative to NO<sub>2</sub> and HCHO  
550 can be recreated by our algorithm, displaying a positive response to both HCHO and NO<sub>2</sub> on the right and  
551 left sides of the ridgelines. This observation underscores the effective parametrization of the non-linearities  
552 in ozone photochemistry achieved through the DNN algorithm. In the subplot representing normal  
553 conditions, we overlaid three lines indicating FNR values of 1.5 (blue), 2.5 (green), and 3.5 (cyan). Souri  
554 et al. (2025) used these lines to determine various coefficients in the PO<sub>3</sub>LASSO parameterization. For  
555 instance, the derivative of PO<sub>3</sub> with respect to NO<sub>2</sub> was determined to be -0.14 ppbv/hr for FNR < 1.5 but  
556 increased to 6.54 ppbv/hr for FNR > 3.5. However, in practice, the thickness and curvature of the PO<sub>3</sub>  
557 isopleths vary based on the prevailing atmospheric conditions, implying that the derivatives cannot  
558 consistently retain the same values across the broad range of conditions.

559 In bright conditions, not only do we observe a significantly accelerated response of PO<sub>3</sub> compared  
560 to the norm at identical NO<sub>2</sub> and HCHO concentrations, but the responses of PO<sub>3</sub> to these two compounds  
561 also become more pronounced. Conversely, in dim conditions, both the magnitudes and responses are  
562 weaker.

563 These results underscore the importance of including photolysis rates in ozone sensitivity analysis,  
564 rather than relying solely on FNR in former studies. For example, a lower FNR in the morning (~0930 LST)  
565 compared to the afternoon may wrongly suggest that PO<sub>3</sub> would become more sensitive to VOCs earlier in  
566 the day. However, decreased light in the morning reduces the sensitivity of PO<sub>3</sub> to VOCs, despite a lower  
567 FNR (Text S1).

568 The contrast between dry and humid isopleths suggests that the presence of H<sub>2</sub>O(v) enhances PO<sub>3</sub>  
569 when abundant NO<sub>2</sub> and HCHO are present. This trend is similarly observed in the F0AM model, as  
570 depicted in Figure S4, indicating that an increase in H<sub>2</sub>O(v) over polluted regions (arbitrarily defined as  
571 HCHO×NO<sub>2</sub> > 10) increases PO<sub>3</sub>. Nonetheless, more humidity suppresses PO<sub>3</sub> especially where VOC is  
572 limited and NO<sub>2</sub> is elevated possibly because the generated OH molecules from O<sup>1</sup>D+H<sub>2</sub>O(v)  
573 predominantly react with elevated NO<sub>2</sub>.

574 Lastly, we see the highest PO<sub>3</sub> rates recorded among all scenarios under a hypothetical condition  
575 characterized by high humidity and photolysis rates. This condition is rare in nature because large amounts  
576 of H<sub>2</sub>O(v) ( $0.8 \times 10^{18}$  molec/cm<sup>3</sup>) are confined to marine regions where surface reflectivity is low;  
577 nonetheless, an intuitive tendency from PO<sub>3</sub>DNN suggests that the algorithm does not create non-physical  
578 extrapolation values.

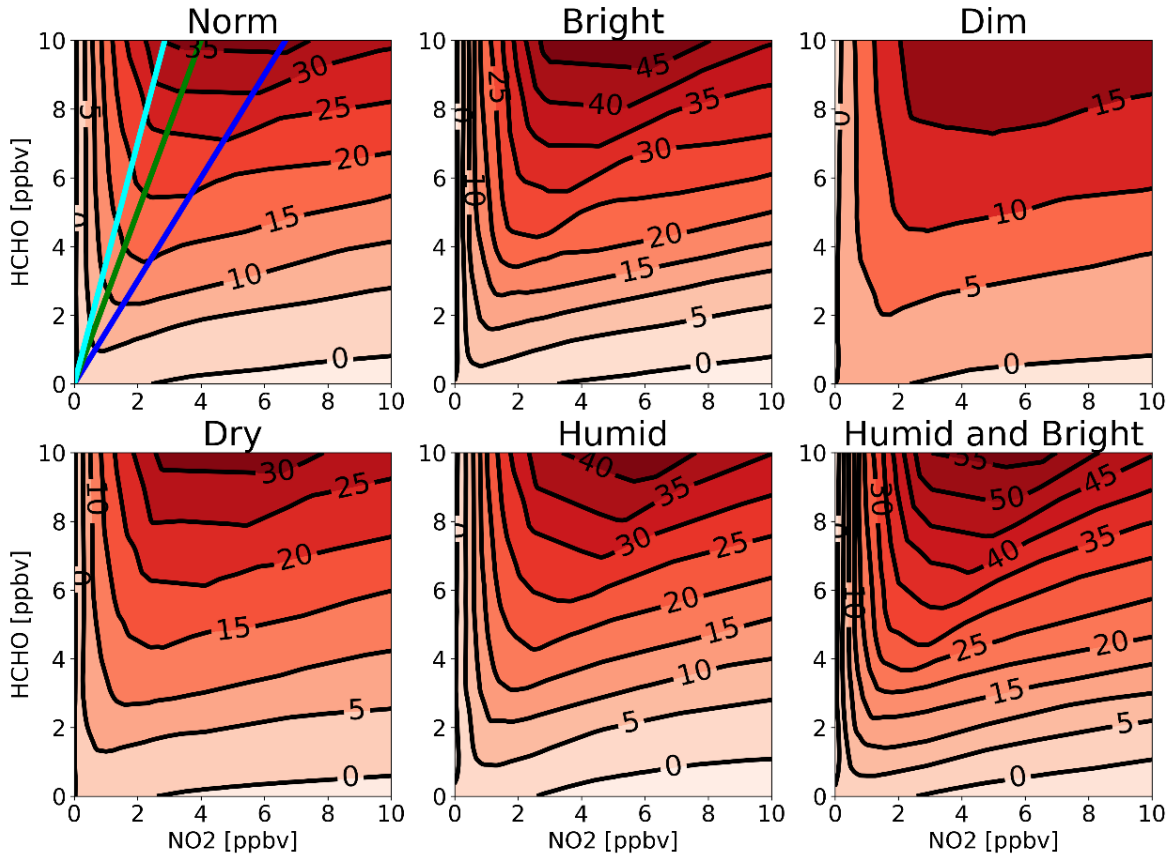
579

580

581       **Table 3.** Six different atmospheric conditions defined to understand the response of PO<sub>3</sub> to HCHO  
582 and NO<sub>2</sub> changes.

Labels	H <sub>2</sub> O [molec/cm <sup>3</sup> ]	jO <sup>1</sup> D [1/s]	jNO <sub>2</sub> [1/s]	Notes
<i>Norm</i>	0.4×10 <sup>18</sup>	4×10 <sup>-5</sup>	1.2×10 <sup>-2</sup>	A typical condition in summer in the eastern US at noon
<i>Bright</i>	0.4×10 <sup>18</sup>	7×10 <sup>-5</sup>	1.4×10 <sup>-2</sup>	Central America with abundant sunshine in the afternoon
<i>Dim</i>	0.4×10 <sup>18</sup>	3×10 <sup>-5</sup>	0.7×10 <sup>-2</sup>	Scandinavia in the afternoon summer
<i>Dry</i>	0.1×10 <sup>18</sup>	4×10 <sup>-5</sup>	1.2×10 <sup>-2</sup>	An arid region such as Spain Meseta Central in the afternoon summer
<i>Humid</i>	0.8×10 <sup>18</sup>	4×10 <sup>-5</sup>	1.2×10 <sup>-2</sup>	A place like Persian Gulf with high humidity and abundant sunshine
<i>Humid and Bright</i>	0.8×10 <sup>18</sup>	7×10 <sup>-5</sup>	1.4×10 <sup>-2</sup>	Since accelerated photolysis rates close-to-surface usually occur over bright regions (arid) with low humidity, this condition is rare in nature.

583



584

585 **Figure 5.** The contour maps of  $\text{PO}_3$  isopleth generated by  $\text{PO}_3\text{DNN}$  algorithm for six different atmospheric  
 586 conditions defined in Table 3. In the first subplot, blue, green, and cyan lines indicate  $\text{FNR}=1.5, 2.5$ , and  
 587 3.5, respectively. Numbers on isopleths are in ppbv/hr.

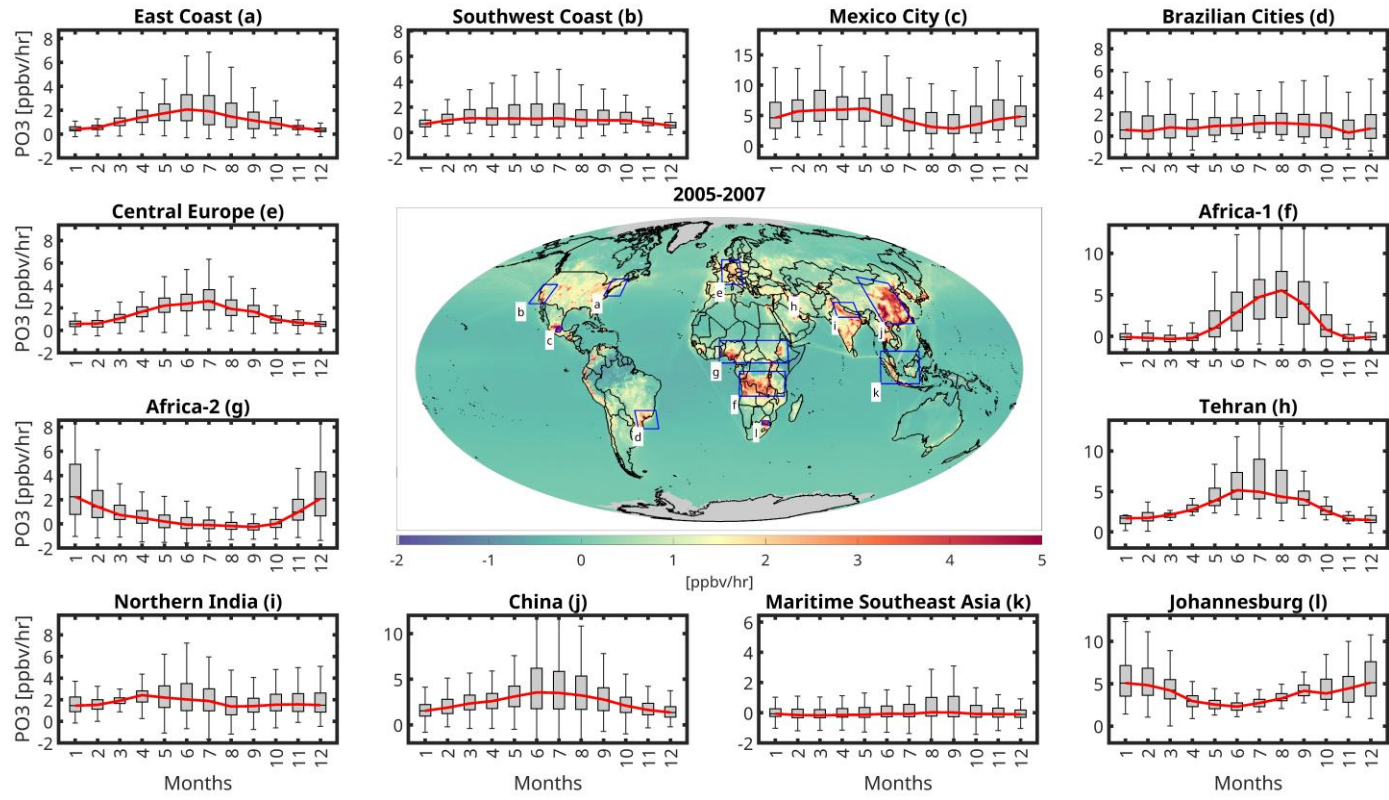
588 **4.4.  $\text{PO}_3$  Maps and Sensitivities using OMI and TROPOMI: A General View, Long-term  
 589 analysis, Intercomparisons, and Error Analysis**

590 **4.4.1. Global  $\text{PO}_3$  and Seasonality using OMI in 2005-2007**

591 Figure 6 shows the global distribution of  $\text{PO}_3$  rates averaged over a quarter-degree in 2005-2007,  
 592 using OMI HCHO and  $\text{NO}_2$  retrievals. It also includes whisker-box plots highlighting seasonal variations  
 593 in  $\text{PO}_3$  for selected regions and cities. We selected the 2005-2007 timeframe for this analysis because the  
 594 OMI data were free from degradation issues, including the row anomaly. The map indicates accelerated  
 595  $\text{PO}_3$  rates across heavily polluted regions, such as cities in the Middle East, Asia, the U.S., Central Europe,  
 596 and Africa, aligning with what we observed in Souri et al. (2025). While some areas exhibit significant  
 597 seasonal fluctuations, others show little variability throughout the seasons. Notably, the east coast of the  
 598 U.S., Central Europe, China, Tehran, and Johannesburg experience peak  $\text{PO}_3$  rates in summer. This pattern  
 599 is primarily attributed to enhanced photochemistry and the elevated sensitivity of  $\text{PO}_3$  to  $\text{NO}_x$ , driven by  
 600 increases in VOC/NO<sub>x</sub> (Souri et al., 2025).

601 The seasonal variability of  $\text{PO}_3$  in two African regions, characterized by biomass burning, exhibits  
 602 an anti-correlation. This occurs because biomass burning in the northern hemisphere of Africa occurs from  
 603 November to March, while the southern hemisphere in Africa experiences it from June to September  
 604 (Roberts et al., 2009). Maritime Southeast Asia also shows a peak in  $\text{PO}_3$  during the biomass burning season  
 605 (August-September).

606 Places like Mexico City, several major Brazilian cities (including Sao Paulo and Rio de Janeiro),  
 607 northern India, and the southwest coast of the U.S. show minimal seasonal variability in  $\text{PO}_3$ . The lack of  
 608 pronounced seasonal changes may be attributed to less pronounced fluctuations in photolysis rates or  
 609 substantial spatial heterogeneity in the seasonal variabilities of HCHO and  $\text{NO}_2$ , resulting in reduced  
 610 seasonal variations but with greater variance. Nonetheless, certain weather conditions can influence these  
 611 results; for instance, monsoon flows can disperse and scavenge pollution from the northern India around  
 612 July-September (David and Nair, 2013), dampening  $\text{PO}_3$ . Mexico City also experiences a monsoon season  
 613 in summer causing pollution to subside temporarily. The attribution of the seasonality will be discussed in  
 614 the next section.



616 **Figure 6.** (center) The averaged global  $\text{PO}_3$  map at  $0.25^\circ \times 0.25^\circ$  in 2005-2007 based on the new algorithm.  
 617 OMI data are used to populate HCHO and  $\text{NO}_2$  abundance. (margins) the whisker-box plots of  $\text{PO}_3$   
 618 seasonality over various selected regions. In the box plot, the central red line shows the median, and the top  
 619 and bottom edges of the box show the 25th (q1) and 75th (q3) percentiles. The dark solid lines at the very  
 620 beginning and the end of each plot show the minimum and maximum values excluding the outliers. The  
 621 outliers are removed based on by any value above  $q3+1.5 \times (q3-q1)$  or below  $q1-1.5 \times (q3-q1)$ .

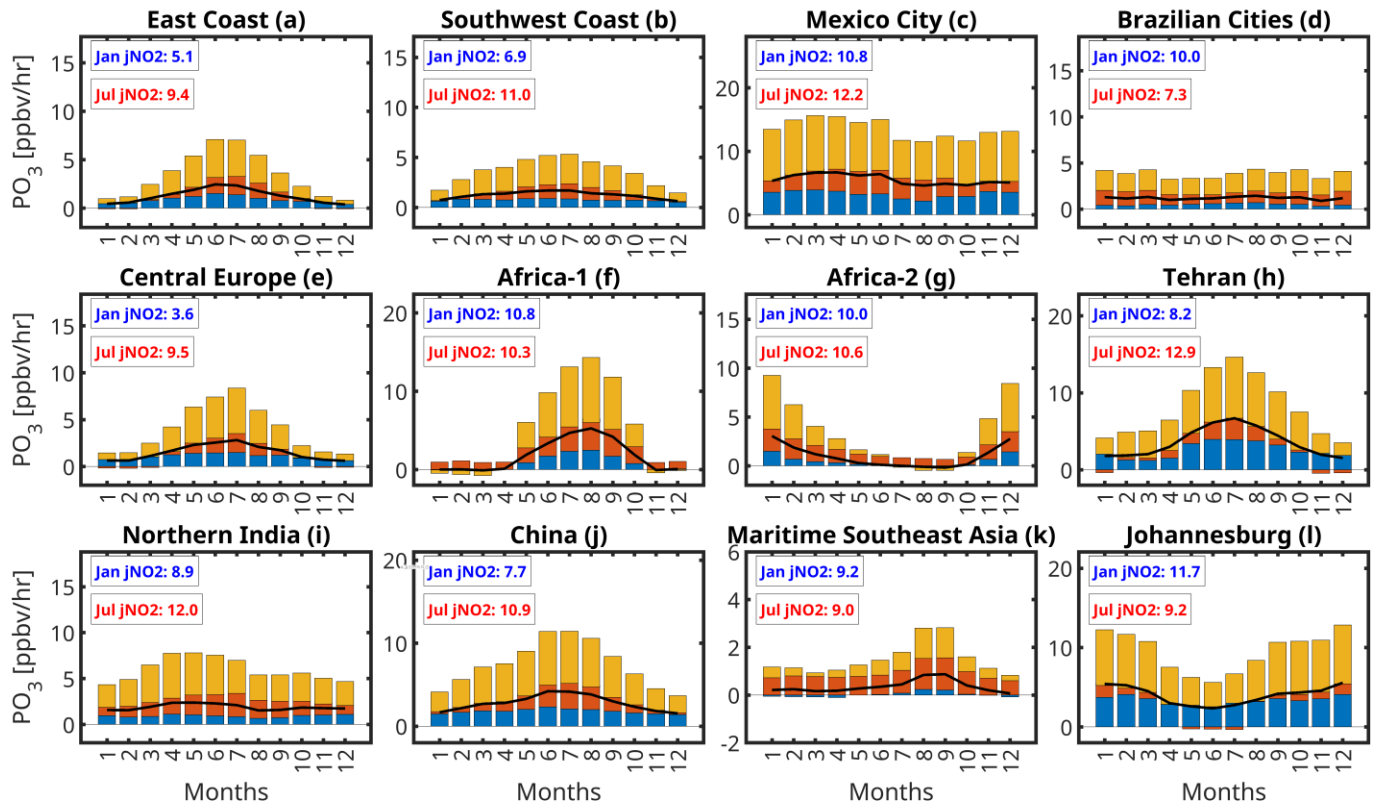
#### 622 4.4.2. The attribution of $\text{PO}_3$ seasonality

623 Figure 7 illustrates the sensitivity of  $\text{PO}_3$  to  $\text{NO}_2$ , HCHO, and combined J-values ( $j\text{NO}_2$  and  $j\text{O}^1\text{D}$ )  
 624 based on Eq.3 across the same regions and months presented in Figure 6. The absolute values of PBL  
 625 HCHO,  $\text{NO}_2$ , and  $j\text{NO}_2$  are shown in Figure S14. As shown in Appendix A, these sensitivity values are  
 626 influenced by both the magnitude of the precursor and the first derivative of  $\text{PO}_3$  with respect to that  
 627 precursor. Thus, the sensitivity values should be interpreted as the result of these combined effects.  
 628 Moreover, these sensitivities are calculated with respect to local HCHO and  $\text{NO}_2$  concentrations rather than  
 629 local emissions (unlike typical modeling experiments). Local concentrations reflect the combined influence

630 of both local and external emissions through various physicochemical processes. We exclude water vapor  
631 from sensitivity analysis because its impact is an order of magnitude smaller than the three other factors.

632 The amplitude of photolysis rates dictates the amplitude of the sensitivity of  $\text{PO}_3$  to  $\text{NO}_2$  and  
633  $\text{HCHO}$ . For instance, over East Coast, Central Europe, and Tehran, the first derivative of  $\text{PO}_3$  to  $\text{NO}_2$  tends  
634 to be small during colder months, primarily because of reduced photochemistry. As a result, despite  
635 significantly higher  $\text{NO}_2$  concentrations in these months, the sensitivity of  $\text{PO}_3$  to  $\text{NO}_2$  is muted. Conversely,  
636 in warmer months, the larger positive derivative of  $\text{PO}_3$  relative to  $\text{NO}_2$ , driven by increased  $\text{HCHO}$  levels  
637 (shifting away from VOC-sensitive regimes) and enhanced photolysis rates, markedly increases the  
638 contributions of low summer  $\text{NO}_2$  levels to  $\text{PO}_3$ . Likewise, we observe substantially higher sensitivity of  
639  $\text{PO}_3$  to  $\text{HCHO}$  concentrations during warmer seasons. This increase is attributed to both the elevated levels  
640 of  $\text{HCHO}$  and the growing derivative of  $\text{PO}_3$  with respect to  $\text{HCHO}$ , both of which are directly influenced  
641 by enhanced photochemistry. One might argue that summer conditions should lead to a shift towards  
642 extremely  $\text{NO}_x$ -sensitive regimes, resulting in a reduced first-order derivative of  $\text{PO}_3$  to  $\text{HCHO}$ . However,  
643 most polluted regions chosen for this figure are in transitional regimes during the summer, which renders  
644  $\text{PO}_3$  fairly responsive to  $\text{HCHO}$  concentrations.

645 The sensitivity of  $\text{PO}_3$  to photolysis rates is dependent on pollution levels, just as its sensitivity to  
646  $\text{HCHO}$  and  $\text{NO}_2$  concentrations is influenced by photolysis rates. This is primary reason for seeing minimal  
647 seasonality of  $\text{PO}_3$  over Mexico City, various Brazilian cities, and northern India. These minimal changes  
648 in photolysis rate sensitivities are caused by the less pronounced seasonality in both photolysis rates and  
649 pollution levels compared to other areas (Figure S3). Souri et al. (2025) found that photolysis rates  
650 significantly contribute to the production of  $\text{PO}_3$  when there is an adequate amount of ozone precursors.  
651 This was reflected in larger (smaller) coefficients associated with photolysis rates in  $\text{PO}_3$ LASSO algorithm  
652 for polluted (pristine) regions. For example, high photolysis rates over the Sahara do not significantly  
653 contribute to  $\text{PO}_3$  because of the limited availability of ozone precursors needed to initiate the  $\text{RO}_x\text{-HO}_x$   
654 cycle. A notable example can be observed in Africa, where photolysis rates tend to remain consistently high  
655 throughout the year under near cloud-free conditions (Figure S14). However, there is a marked seasonality  
656 in the sensitivity of  $\text{PO}_3$  with respect to photolysis rates during polluted months suggesting that the ample  
657 precursors can leverage available lights to form more ozone molecules. This pattern underscores the  
658 algorithm's capability to understand the intertwined relationships between the photolysis rate sensitivities  
659 and pollution levels, as well as the pollution sensitivities and photolysis rates.



661 **Figure 7.** The bar plots of the sensitivity of PO<sub>3</sub> to photolysis rates, NO<sub>2</sub>, and HCHO concentrations within  
662 the PBL over the selected regions shown in Figure 6. These sensitivities are influenced by both the  
663 magnitude of the precursors and the first-order derivative of PO<sub>3</sub> to the precursor, detailed in Appendix A.  
664 jNO<sub>2</sub> values are in  $1 \times 10^{-3}/\text{s}$  units.

#### 665 4.4.3. Global PO<sub>3</sub> linear trends using OMI (2005-2019)

666 Using the linear trend calculation method outlined by Souri et al. (2024), we compute global long-  
667 term linear trends of PO<sub>3</sub> from OMI data, shown in Figure 8. High-latitude regions ( $>65^\circ$ ) are excluded due  
668 to limited photochemical activity. We observe large variability in both the signs and magnitudes of the linear  
669 trends. Predominantly positive trends occur over the Middle East, India, and China, while negative trends  
670 are mostly found in the eastern U.S., southern parts of Europe, maritime Southeast Asia, and several areas  
671 in Africa. The largest upward trend in PO<sub>3</sub> over the U.S. occurs in oil and gas producing regions, including  
672 the Permian Basin. While various physicochemical processes beyond near-surface PO<sub>3</sub> influence  
673 tropospheric ozone trends, the strong agreement between predominantly upward PO<sub>3</sub> trends in Asia and the  
674 Middle East suggested by satellite-based ozone observations (Gaudel et al., 2018; Boynar et al., 2025) is  
675 noteworthy.

676 To gather a more relative perspective, Figure 9 shows relative PO<sub>3</sub> trends (as percentages relative  
677 to 2005 annual averages) for regions where PO<sub>3</sub> exceeds 0.5 ppbv/hr. The largest relative changes (>30%)  
678 are evident over the Persian Gulf, Chile, India, and China. Large negative values dominate over the eastern  
679 U.S. and over the central Africa (>20%).

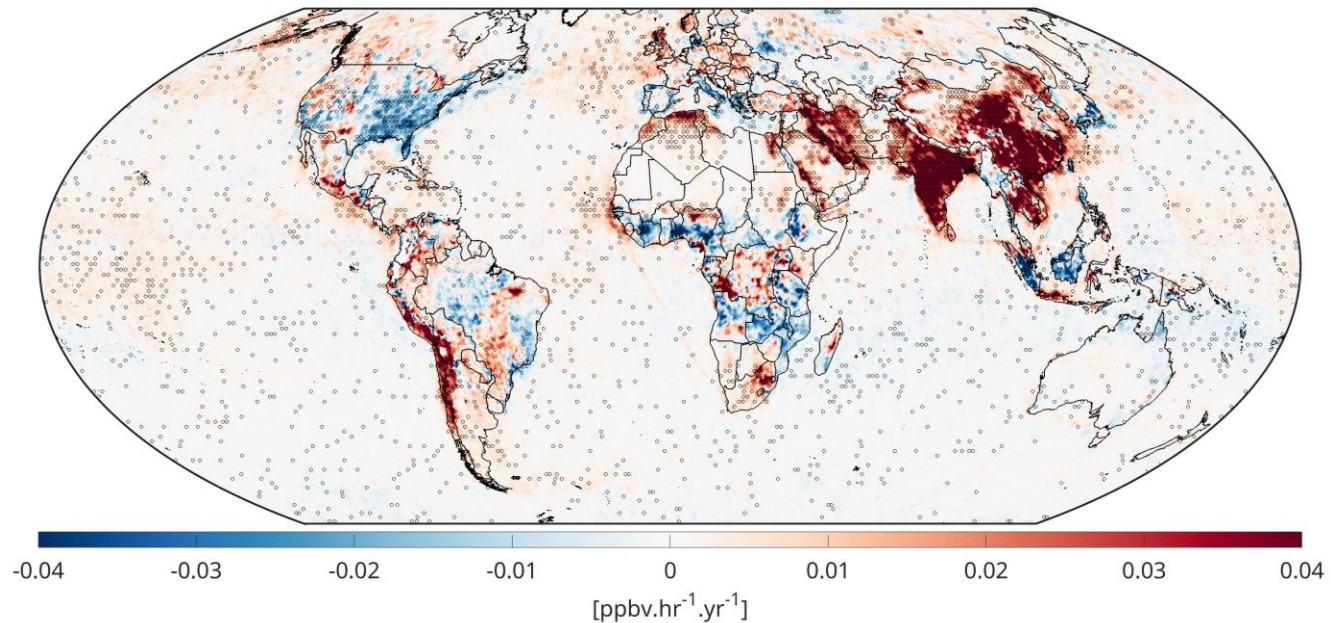
680 Multiple factors in our parameterization can simultaneously influence these trends, including  
681 changes in HCHO VCDs, NO<sub>2</sub> VCDs, dynamic changes in column-to-PBL conversion factors from  
682 MINDS, water vapor, and photolysis rates. However, photolysis rate trends should be negligible because  
683 long-term changes in total overhead ozone are insignificant at midlatitudes (Figure S2 in Souri et al., 2024),

684 and surface albedo is based on a monthly climatology dataset. While water vapor increases over time in  
685 response to global warming (Souri et al., 2024; Borger et al., 2024), these changes are insufficient to explain  
686 the large variability in  $\text{PO}_3$  linear trends over polluted regions. Accordingly, simultaneous changes in HCHO  
687 and  $\text{NO}_2$  boundary layer mixing ratios are the main drivers of  $\text{PO}_3$  trends.

688 The  $\text{PO}_3$  trends are generally explained by changes in ozone precursor concentrations which are  
689 mapped in Figures S15 and S16. The attribution of trends in OMI HCHO and  $\text{NO}_2$  have been partly  
690 discussed in Souri et al., 2024 and the references therein. Increases in both HCHO and  $\text{NO}_2$  over the Middle  
691 East, India, and China drive rising  $\text{PO}_3$  over time. Conversely, reduced HCHO and  $\text{NO}_2$  concentrations over  
692 parts of Africa, the eastern U.S., and maritime Southeast Asia, have led to  $\text{PO}_3$  reductions. However, many  
693 localized areas exhibit strong non-linearity. For instance, Tehran (Iran) shows positive  $\text{PO}_3$  trends caused  
694 by  $\text{NO}_2$  increases in a predominantly VOC-sensitive regime, reducing ozone loss through  $\text{NO}_2+\text{OH}$   
695 reactions. Los Angeles (USA) shows upward trends attributed to rapid  $\text{NO}_2$  reductions, resulting in the  
696 opposite effect (Text S2)

697 The quantitative characterization of these trends (similar to our analysis of  $\text{PO}_3$  seasonality in  
698 Section 4.4.2 or rapid  $\text{PO}_3$  changes during a heatwave in Text S3) presents significant challenges for several  
699 reasons: (i) the amplitudes of these trends are generally an order of magnitude smaller than seasonal  
700 changes, requiring more stringent attribution methods, (ii) the sensitivities of  $\text{PO}_3$  to input parameterization  
701 can behave non-linearly, making a linear trend analysis ill-suited for some localized areas, and (iii) changes  
702 in ozone precursors have effects on the sensitivity of  $\text{PO}_3$  to photolysis rates as described in Section 4.4.2,  
703 introducing a convoluted problem.

704 Since our  $\text{PO}_3$  parameterization encapsulates non-linear and interdependent relationships between  
705 pollution levels, light intensity, and water vapor, fully isolating individual effects on  $\text{PO}_3$  trends requires  
706 reproducing the product while holding either  $\text{NO}_2$  or HCHO constant individually and allowing others to  
707 evolve over time (an approach similar to modeling experiments in Souri et al., 2024). This approach  
708 comprehensively captures the non-linear dependencies between input variables and  $\text{PO}_3$ , circumventing the  
709 need for crude linear approximations.

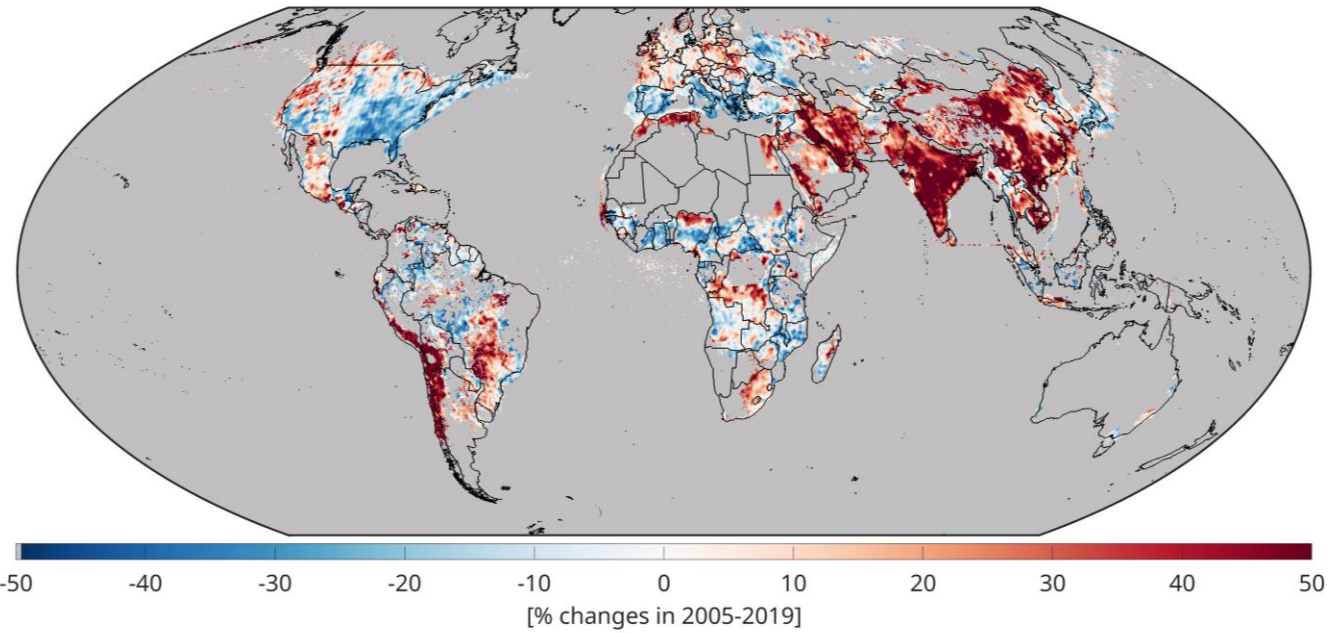


710

711 **Figure 8.** The linear trend maps of  $\text{PO}_3$  within PBL derived from our new algorithm using OMI in 2005-  
712 2019. Dots indicate that the trend has passes a statistical test based on the Mann-Kendall test at 95%  
713 confidence interval.

714

715



716

717 **Figure 9.** Similar to Figure 8 but percentage changes are instead shown over  $\text{PO}_3 > 0.5 \text{ ppbv/hr}$ .

#### 718 4.4.4. High resolution TROPOMI-based $\text{PO}_3$ maps contrasted with OMI in 2019

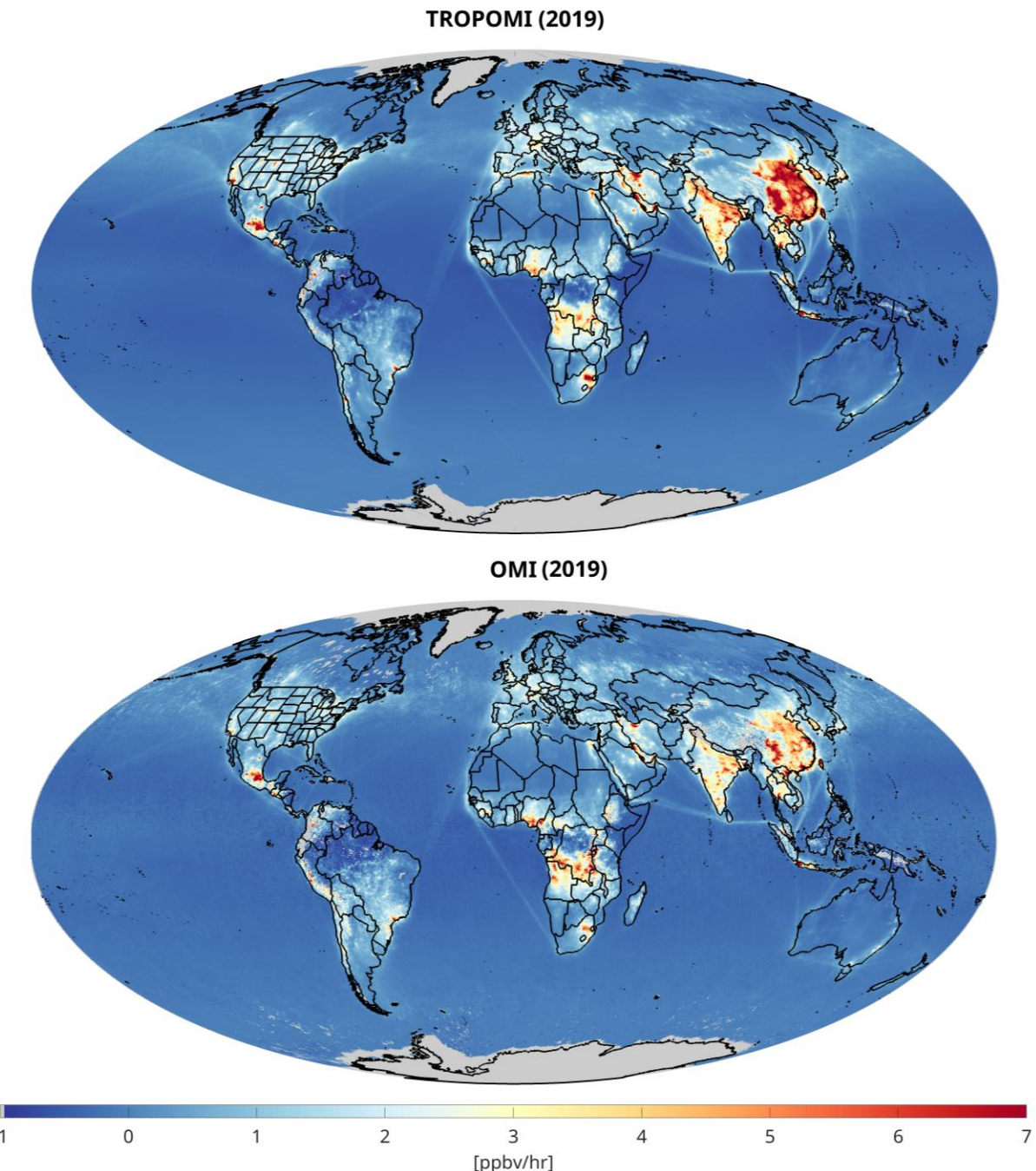
719 Accelerated rates of  $\text{PO}_3$  at approximately 1330 LST are observed consistently across polluted  
720 midlatitude regions characterized by high photolysis rates. This pattern is substantiated by the global  $\text{PO}_3$   
721 maps derived from TROPOMI and OMI data for the year 2019 illustrated in Figure 10. While the maps  
722 presented are averages for 2019, significant  $\text{PO}_3$  hotspots (exceeding 8 ppbv/hr) are identified over  
723 metropolitan/industrial areas including Mexico City (Mexico), Tehran (Iran), the Persian Gulf, and Hunan  
724 Province (China). There are less documented regions undergoing elevated locally-produced ozone such as  
725 Johannesburg (South Africa), Rio de Janeiro (Brazil), Sao Paulo (Brazil), and Santiago (Chile). In contrast,  
726 Europe emerges as a region with comparatively low  $\text{PO}_3$  levels despite its dense population. This tendency  
727 may be attributed to lower photolysis rates (characterized by high solar zenith angles and low surface  
728 reflectivity) as well as effective emissions mitigation strategies. A notable similarity exists between these  
729 identified hotspots and those reported by Souri et al. (2025), although the contrast between clean and  
730 polluted areas is more pronounced in the  $\text{PO}_3$ DNN product because of an improved representation of  
731  $\text{PO}_3$ DNN in clean regions.

732  $\text{PO}_3$  exhibits a slight negative value over oceanic and densely forested areas (such as the Amazon  
733 and Congo), primarily because of ozone sinks associated with water vapor ( $\text{H}_2\text{O}(v)$ ) and alkenes, which are  
734 implicitly included in our parametrization. However, a marked contrast is observed between the slightly  
735 negative and positive  $\text{PO}_3$  levels along marine vessel pathways. These ship paths are informed not only by  
736 remote sensing data (Georgoulias et al., 2020) but also by the conversion of column measurements to PBL  
737 mixing ratios thorough the MINDS simulation, which accounts for ship emissions. Given that the PBL is

738 typically shallow over marine regions, the conversion factor is expected to be substantial for these  
739 pathways, resulting in a pronounced contrast in pollution levels.

740 The finer spatial resolution of the TROPOMI dataset enhances the detail of the PO<sub>3</sub> maps compared  
741 to those derived from OMI, yielding less noise and fuller data. This reduction in gaps in TROPOMI-based  
742 PO<sub>3</sub> is attributed to a lower likelihood of cloud contamination and the full coverage of all pixels in the  
743 detector, in contrast to OMI, which suffers from the row anomaly. Visual analysis of the two datasets  
744 indicates that TROPOMI often shows higher PO<sub>3</sub> than OMI over polluted regions. Except for NO<sub>2</sub> and  
745 HCHO VCDs, the inputs to the parametrization are identical across both products.

746 To further investigate these differences, we synchronize the TROPOMI datasets at the OMI-based  
747 spatial resolution and produced scatterplots, as displayed in Figure 11. The correspondence between the  
748 two products is high ( $R^2 = 0.86$ ). Nonetheless, TROPOMI-based PO<sub>3</sub> levels are approximately 10% greater  
749 than those derived from OMI. The fact that we observe this overestimation given that TROPOMI has been  
750 coarsened to match OMI's footprint suggests that the differing spatial resolutions (0.25 degrees versus 0.1  
751 degrees) are unlikely to account for the discrepancy. Moreover, we undertake a comparative analysis of  
752 NO<sub>2</sub> and HCHO mixing ratios within the PBL region as obtained from MINDS alongside these two satellite  
753 datasets. Given that the conversion factor remains consistent between the two products, any observed  
754 differences can be attributed to variations in their respective VCDs. Our analysis reveals that both NO<sub>2</sub> and  
755 HCHO mixing ratios are higher in TROPOMI relative to OMI (by 5-6%), thereby providing a good  
756 explanation for higher TROPOMI-based PO<sub>3</sub> in comparison to OMI.

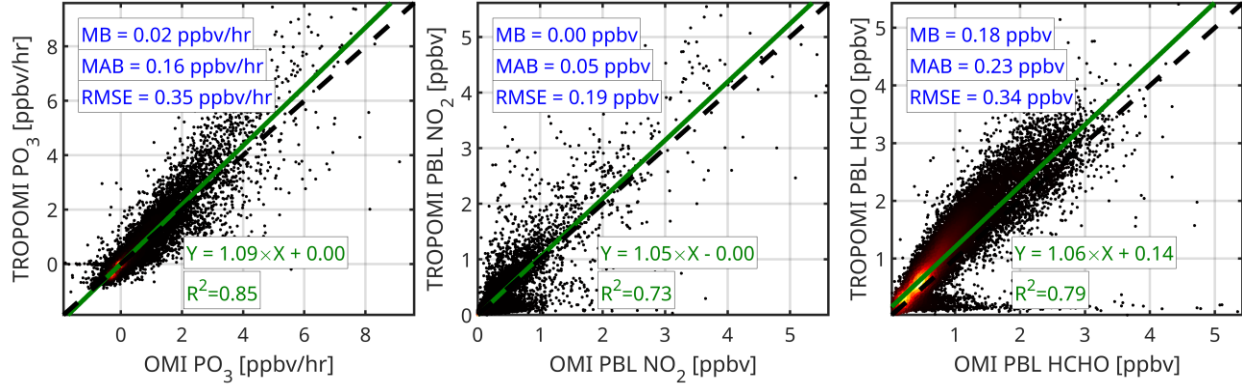


757

758 **Figure 10.** Global maps of  $\text{PO}_3$  derived from TROPOMI (top) and OMI (bottom) datasets based on the  
 759  $\text{PO}_3\text{DNN}$  algorithm in 2019. These values are estimated within the PBL region at  $\sim 1330$  LST. The data  
 760 exclude cloudy pixels, strong smoke, sensor anomalies, and snow based on the recommended quality flags  
 761 coming with TROPOMI and OMI products.

762

763



764

765 **Figure 11.** Scatterplots of (left) OMI PO<sub>3</sub> vs. TROPOMI PO<sub>3</sub>, (middle) OMI PBL NO<sub>2</sub> vs. TROPOMI PBL  
 766 NO<sub>2</sub>, and (right) OMI PBL HCHO vs. TROPOMI PBL HCHO based on 2019. We coarsen TROPOMI  
 767 dataset to match OMI's spatial resolution to remove the effect of spatial footprint on these results.

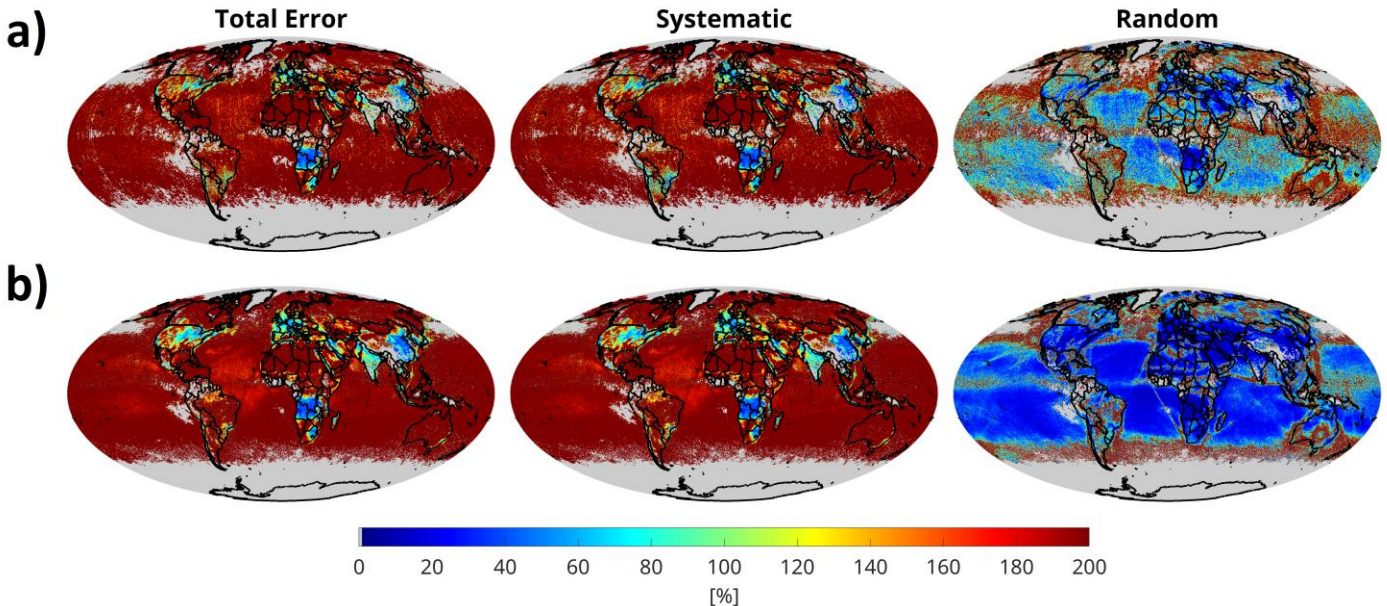
768 *4.4.5. Error Analysis*

769 Based on the formulation outlined in Section 3.4, we evaluate both the systematic and random error  
 770 components of PO<sub>3</sub> for July 2019, based on data from both OMI and TROPOMI retrievals. Figure 12  
 771 presents the average error values for the month. Total PO<sub>3</sub> errors range from 25% to 80% in areas  
 772 characterized by moderate to extreme pollution, while in more remote regions, errors can surpass 200%.

773 On average, random errors constitute only a small fraction of the total error budget, with OMI  
 774 showing consistently larger random errors than TROPOMI across the region. This is primarily a result of  
 775 OMI's limited sampling caused by row anomaly issues. As mentioned in Section 4.2, these random errors  
 776 are significantly lower when compared to the PO<sub>3</sub>LASSO random errors (Souri et al., 2025).

777 Systematic errors account for most of the total error, exceeding 90%. These systematic errors are  
 778 comprised of three components: biases arising from the correction of VCDs using ground-based remote  
 779 sensing data, errors related to DNN predictions, and conversion factors derived from the MINDS  
 780 framework. The first two components contribute minimally to the overall error (less than 5%), making the  
 781 MINDS conversion factors the dominant contributor to the total error budget. Therefore, any  
 782 parametrization aimed at converting satellite-based VCDs to near-surface concentrations, including the one  
 783 presented in this study, should always seek out a model that accurately reflects the shape of the profiles.

784 We also quantify the impact of inconsistent shape factors used in the retrievals and the MINDS  
 785 profile on PO<sub>3</sub> estimates and find them introducing systematic errors of 5-25% over PO<sub>3</sub>>0.5 ppbv/hr  
 786 (Figures S17-S20). Refining TROPOMI and OMI products with MINDS shape factors would require  
 787 reproducing several large-scale validation efforts (e.g., Verhoelst et al., 2021; Vigouroux et al., 2020;  
 788 Pinardi et al., 2021; Ayazpour et al., 2025), which is beyond the practical scope and resources of this study.

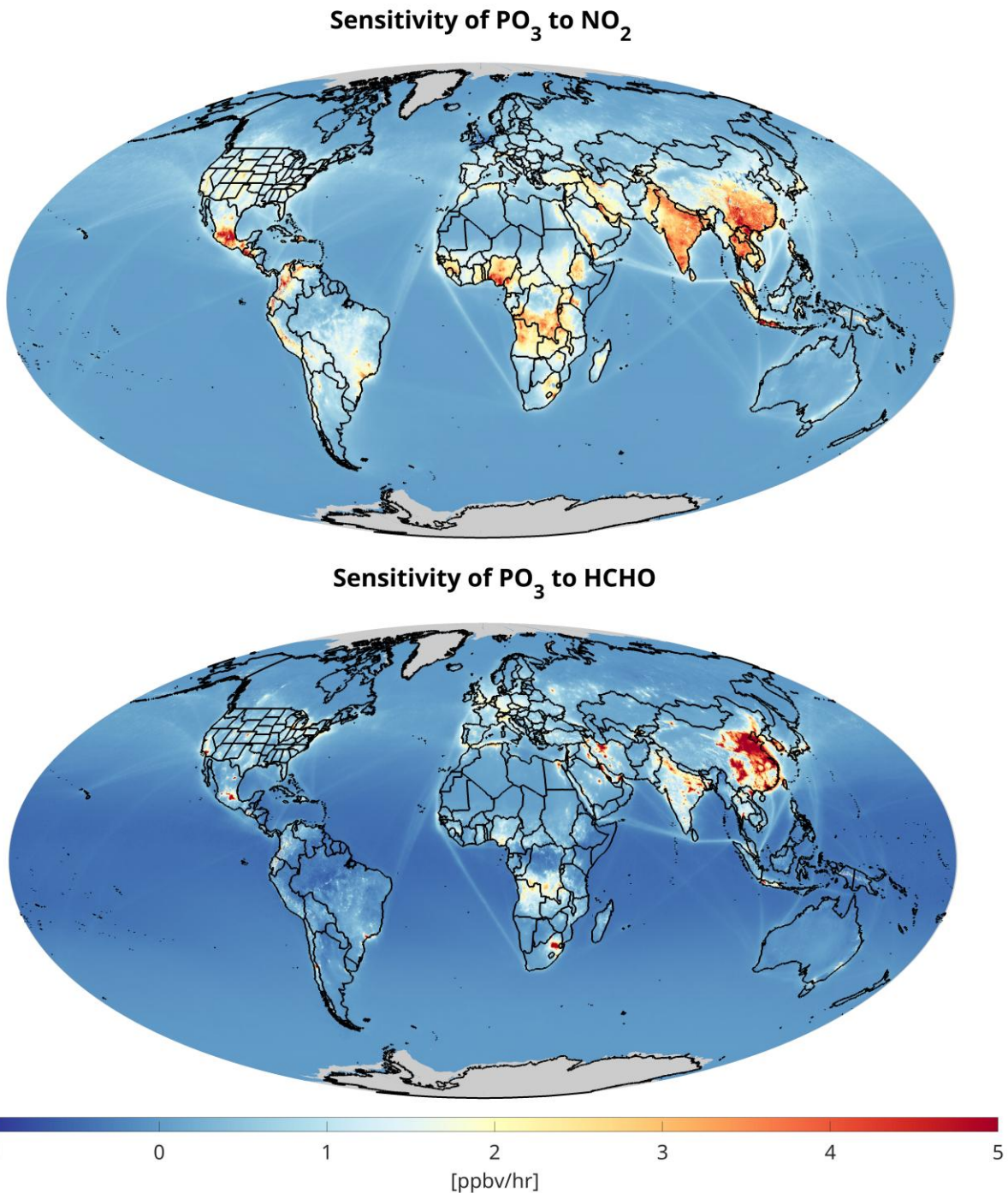


789  
 790 **Figure 12.** The maps of total error, systematic, and random errors for (a) OMI, and (b) TROPOMI  
 791 computed for July 2019.

792 *4.5.6. Beyond binary maps obtained from FNR: Ozone sensitivity maps using high-resolution TROPOMI*  
 793 data

794 We explore the spatially varying sensitivity of  $\text{PO}_3$  to  $\text{HCHO}$  and  $\text{NO}_2$  worldwide using TROPOMI.  
 795 These maps provide finer information compared to binary maps obtained from FNRs. Figure 13 illustrates  
 796 global maps of these sensitivities averaged for the year 2019. We observe negative sensitivity values of  $\text{PO}_3$   
 797 to  $\text{NO}_2$  in urban areas, which aligns with our understanding of non-linear ozone chemistry. These negative  
 798 values are particularly pronounced in northern China, where  $\text{VOCR/NO}_x$  ratios remain low throughout the  
 799 year. Similar non-linear feedback patterns can be seen in the Benelux region and the United Kingdom,  
 800 primarily driven by elevated  $\text{NO}_2$  levels. In contrast,  $\text{NO}_2$  significantly contributes to higher  $\text{PO}_3$  in southern  
 801 China, India, Mexico, and several regions across Africa.

802 As indicated in Souri et al. (2025), the influence of  $\text{HCHO}$  on  $\text{PO}_3$  is largely governed by  $\text{NO}_x$   
 803 emissions. This relationship explains why the sensitivity of  $\text{PO}_3$  to  $\text{HCHO}$  closely mirrors global  $\text{NO}_2$  levels,  
 804 which dictates the locations of VOC-sensitive regimes. We observe slightly negative sensitivity of  $\text{PO}_3$  to  
 805  $\text{HCHO}$  in remote and densely vegetated regions, likely a result of the effects of alkenes on ozone. However,  
 806 the implicit nature of DNN makes it challenging to identify the exact chemical reasons behind these  
 807 patterns. Noteworthy examples of areas where  $\text{PO}_3$  is significantly influenced by  $\text{HCHO}$  include eastern  
 808 China, Los Angeles (USA), Tehran (Iran), Mexico City (Mexico), and Johannesburg (South Africa).



809

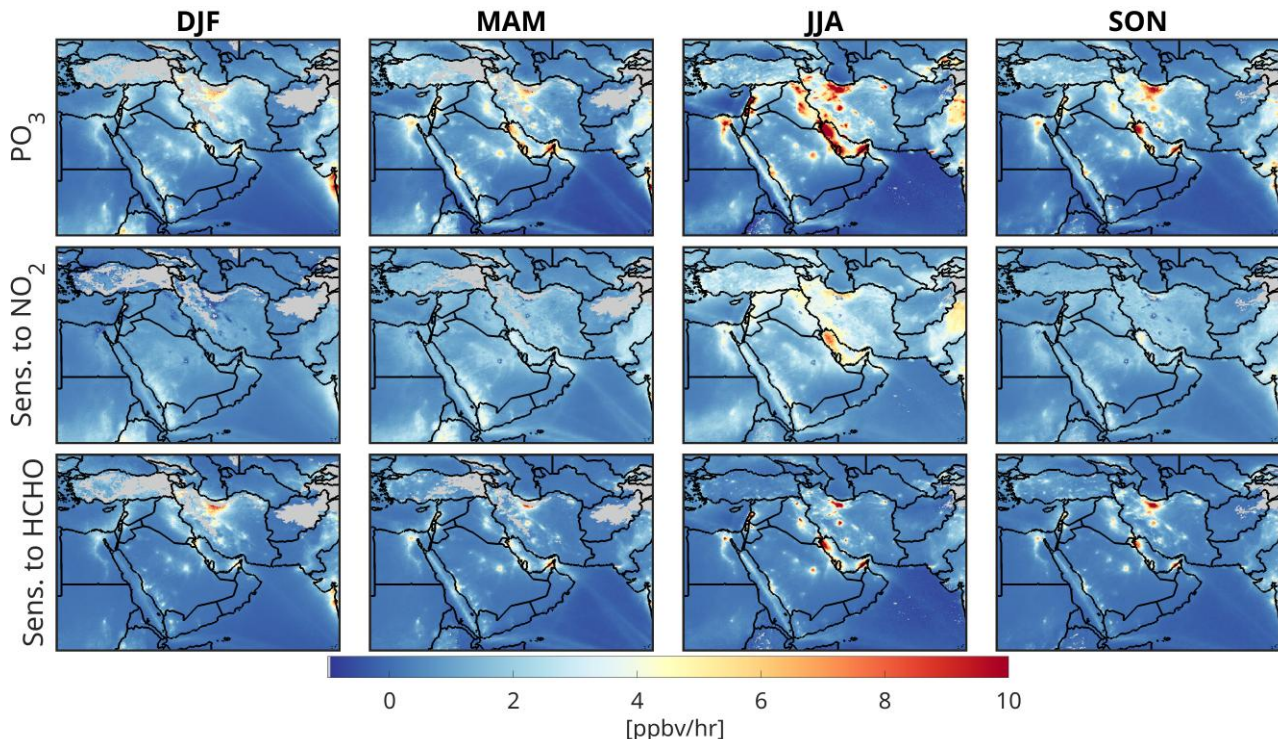
810 **Figure 13.** The sensitivity of  $\text{PO}_3$  to  $\text{NO}_2$  (top) and  $\text{HCHO}$  (bottom) based on our algorithm using  
811 TROPOMI data in 2019.

812

813

814       Figure 14 presents the maps of  $\text{PO}_3$  along with sensitivities across four seasons in 2019 over Middle  
 815       East, derived from TROPOMI data. Notably,  $\text{PO}_3$  values surge during the summer months in several densely  
 816       populated and industrial regions of the Middle East. Furthermore, we observe considerable  $\text{PO}_3$  values in  
 817       the fall, primarily caused by the influence of HCHO. This fall peak is consistent with the observations made  
 818       by Souri et al. (2025), who reported a sharp rise in  $\text{PO}_3$  in late fall 2019 over Tehran (Iran). The overall  
 819       seasonality of  $\text{PO}_3$  is well aligned with the discussions presented in Section 4.4.1. The sensitivity of  $\text{PO}_3$  to  
 820        $\text{NO}_2$  exhibits notable variation, shifting from low and negative values during the colder months to positive  
 821       and high values in the warmer months. We identify HCHO as the predominant contributor to  $\text{PO}_3$  in these  
 822       regions, as the majority of these cities fall in VOC-sensitive environments and emit significant amounts of  
 823       anthropogenic HCHO, whether from primary or secondary sources.

824       These maps eliminate the need for binarization of chemical conditions, as they effectively illustrate  
 825       the spatial variability in ozone response to HCHO and  $\text{NO}_2$  while accounting for light and humidity, two  
 826       important dimensions missing in FNR-based ozone sensitivity diagnosis. A more detailed discussion about  
 827       FNR's inability to fully describe ozone chemistry is documented in Text S1.



828  
 829       **Figure 14.** The magnitude of  $\text{PO}_3$  and the corresponding sensitivity to  $\text{NO}_2$  and HCHO over Middle East  
 830       grouped into four different seasons. DJF: December-January-February, MAM: March-April-May, JJA:  
 831       June-July-August, and SON: September-October-November. *Sens.* means sensitivity.

## 832       5. Summary

833       Early data-driven analyses of ozone chemistry sensitivity primarily relied on "ratio-based"  
 834       indicators to partially linearize the non-linear aspects of urban ozone chemistry, which are influenced by  
 835       pollution levels, light, and water vapor. With the development of more sophisticated algorithms, including  
 836       machine learning techniques capable of fitting high-dimensional non-linear functions, we have shown that  
 837       a highly effective parameterization of net ozone production rates ( $\text{PO}_3$ ) can be achieved. This approach not  
 838       only eliminates the need for empirical linearization of ozone chemistry through various indicators, but it  
 839       also allows for the primary inputs to be accurately constrained using satellite observations. This

840 advancement allowed us to move beyond the previously employed formaldehyde-to-nitrogen dioxide ratio  
841 (FNR) and to generate more comprehensive sensitivity maps, which account for variations not only in  
842 HCHO and NO<sub>2</sub> but also in light and water vapor.

843 We significantly enhanced the empirical parametrization of PO<sub>3</sub> described in Souri et al. (2025), in  
844 several key ways: (i) we improved the representation of PO<sub>3</sub> in both polluted and clean areas using a L2-  
845 regularized deep neural network (DNN) and eliminated the need for empirical linearization of atmospheric  
846 conditions with the FNR approach, resulting in reduced complexity and noise in the final estimates; (ii) we  
847 used a finer, up-to-date global transport model called MINDS to convert satellite-retrieved vertical column  
848 density (VCD) into planetary boundary layer (PBL) mixing ratios; (iii) we incorporated the error from these  
849 conversion factors, derived from comprehensive validation against aircraft spirals, into the total error  
850 budget; and (iv) we generated long-term records of PO<sub>3</sub> magnitudes and sensitivities to nitrogen dioxide  
851 (NO<sub>2</sub>) and formaldehyde (HCHO) using bias-corrected data from the Ozone Monitoring Instrument (OMI)  
852 for the years 2005-2019 (at a resolution of 0.25° × 0.25°) and the TROPOspheric Monitoring Instrument  
853 (TROPOMI) for 2018-2023 (at a resolution of 0.1° × 0.1°). These datasets were collected under partially  
854 cloud-free conditions around 13:30 equatorial local standard time. The two products show strong  
855 agreement, with TROPOMI-based PO<sub>3</sub> being approximately 10% higher than OMI, which is attributed to  
856 higher NO<sub>2</sub> and HCHO concentrations noted by TROPOMI.

857 The DNN algorithm (PO<sub>3</sub>DNN) accounted for more than 96% of the variance in both the test and  
858 training datasets derived from observationally-constrained box simulations across various atmospheric  
859 composition campaigns, with a slope close to the unity line. The new algorithm improved the representation  
860 of PO<sub>3</sub> in remote regions compared to the version developed in Souri et al. (2025), due to the inclusion of  
861 water vapor and the use of a more robust regression model. We found PO<sub>3</sub>DNN to be logically responsive  
862 to its inputs during various idealized experiments that involved changing light conditions, pollution levels,  
863 and water vapor.

864 Expectedly, our results indicate that PO<sub>3</sub> magnitudes and sensitivity maps are primarily influenced  
865 by the levels of ozone precursors, non-linearity of ozone chemistry, and photolysis rates. We revisited the  
866 accelerated PO<sub>3</sub> observed in Souri et al. (2025) across polluted areas, such as major cities and during  
867 biomass burning activities in photochemically active environments. Using sensitivity calculations derived  
868 from the new algorithm, we investigated the contributors to PO<sub>3</sub> seasonality around the globe. We found  
869 that photolysis rates were the primary drivers of PO<sub>3</sub> seasonality. During darker months, both the magnitude  
870 of PO<sub>3</sub> and its sensitivity to NO<sub>2</sub> and HCHO decrease due to limited light availability to initiate the RO<sub>x</sub>-  
871 HO<sub>x</sub> cycle. This critical trend is not represented by the pollution levels alone, highlighting the necessity of  
872 including photolysis rates in ozone sensitivity analyses. Fortunately, we can largely constrain these rates  
873 using satellite observations. In regions with minimal variability in photolysis rates (such as the tropics),  
874 pollution levels became the main driver of PO<sub>3</sub> seasonality.

875 The long record of stable observations from OMI allowed us to generate the first-ever maps of PO<sub>3</sub>  
876 linear trends from 2005 to 2019 globally. The global long-term trends revealed substantial spatial variability,  
877 with predominantly positive trends over Asia and the Middle East (>30% relative to 2005 in some regions)  
878 and negative trends across the eastern U.S., Europe, and parts of Africa. Analysis indicated that  
879 simultaneous changes in HCHO and NO<sub>2</sub> boundary layer concentrations were the primary drivers of these  
880 trends. Although increases in both precursors over Asia and the Middle East, rising PO<sub>3</sub> and reduced  
881 concentrations elsewhere lead to PO<sub>3</sub> decreases, localized non-linearities complicated this relationship, as  
882 demonstrated by contrasting chemical regimes in Tehran vs. Los Angeles. Quantitative attribution of these  
883 trends presents challenges because of their small amplitudes relative to seasonal variations and non-linear  
884 sensitivities in the parameterization, necessitating “hold-one-out” approaches that account for complex  
885 interdependencies between input variables.

886 We error characterized both systematic and random errors associated with PO<sub>3</sub>DNN for both OMI  
887 and TROPOMI-based products. We showed that total errors range from 25% to over 200%, with smaller

888 errors in polluted areas. Random errors are minor on monthly-basis, with OMI exhibiting larger errors due  
889 to row anomaly issues. Systematic errors exceed 90% of the total error, primarily driven by MINDS  
890 conversion factors. The total errors budget emphasizes on the role of model used for converting satellite-  
891 based VCDs to near-surface concentrations and its importance for precisely determining ozone precursors  
892 levels near to the surface. Furthermore, in future efforts, we also need to refine satellite retrievals using  
893 spatially higher-resolution AMFs derived from MINDS while simultaneously performing retrieval  
894 validation against ground-based remote sensing observations.

895 We developed a novel product aimed at enhancing our understanding of the variability in  $\text{PO}_3$  and  
896 its interactions with  $\text{NO}_x$  and VOCs on a global scale. This advanced algorithm has undergone meticulous  
897 tuning and training using an extensive dataset derived from a reliable box model, which is further  
898 constrained by intensive atmospheric composition campaigns conducted by NASA and NOAA. The  
899 algorithm not only yields accurate estimates of  $\text{PO}_3$  with minimal bias in comparison to observationally-  
900 constrained values but also facilitates the derivation of  $\text{PO}_3$  in relation to  $\text{HCHO}$  and  $\text{NO}_2$ . However, as  
901 indicated by Souri et al. (2025), there remain several opportunities for further improvement, including: i)  
902 the incorporation of heterogeneous chemistry; ii) consideration of the impact of partially cloudy regions  
903 and aerosols on photolysis rates; iii) gauging the potential benefits of using more sophisticated chemical  
904 mechanisms for the generation of the training dataset; and iv) enhanced representation of vertical profiles  
905 of  $\text{NO}_2$  and  $\text{HCHO}$  using observationally-constrained chemical transport models with more rigorous  
906 column to near-surface conversion methods (Cooper et al. 2020). Some of these enhancements present  
907 significant challenges, particularly the fine-resolution three-dimensional characterization of aerosol and  
908 cloud properties on a global scale, which is not obtainable with current reanalysis data. However, with the  
909 advent of newer satellite technologies such as PACE and MAIA, there may be opportunities to improve the  
910 representation of atmospheric models with respect to cloud and aerosol characteristics.

911 While the OMI- and TROPOMI-based  $\text{PO}_3$  products maintain algorithmic consistency in several  
912 key components, including photolysis rates and water vapor calculations, the underlying satellite retrievals  
913 of  $\text{HCHO}$  and  $\text{NO}_2$  VCDs remain unharmonized between the two instruments. To address the resulting  
914 inter-instrument biases, we implemented bias correction using ground-based remote sensing retrievals as  
915 reference standards. This approach achieved OMI and TROPOMI  $\text{PO}_3$  agreement within 10% on average.  
916 However, this level of consistency may be insufficient for robust joint trend analysis of the combined OMI-  
917 TROPOMI  $\text{PO}_3$  record over areas with non-linear or minor trends, potentially requiring the implementation  
918 of trend harmonization algorithms (e.g., Hilboll et al., 2013) to ensure statistical reliability in long-term  
919 analyses.

920 The emergence of novel geosynchronous orbit (GEO) technologies is becoming increasingly  
921 important for monitoring the daylight hourly variability in ozone precursors. In particular, the finer spatial  
922 and temporal resolution offered by the Tropospheric Emissions: Monitoring of Pollution (TEMPO),  
923 Geostationary Environment Monitoring Spectrometer (GEMS), and Sentinel-4 instruments will aid in  
924 distinguishing exceptional events from typical atmospheric conditions. In light of the success of emission  
925 mitigation strategies over high income countries, the occurrences of elevated  $\text{PO}_3$  are becoming more  
926 infrequent, thereby necessitating a more detailed and rapid observational strategy for monitoring such  
927 events. This presents a timely opportunity to address ozone exceedance events using TEMPO in conjunction  
928 with our  $\text{PO}_3$  estimator, especially since the algorithm is designed to handle light-limited conditions—such  
929 as those encountered during early morning and late afternoon periods when TEMPO collects data—  
930 conditions that are not feasible to analyze via the FNR approach.

### 931 **Appendix A: The sensitivity maps are the directional derivative**

932 To demonstrate that the sensitivity calculation of  $\text{PO}_3$  to its inputs resembles (Eq.3) a directional derivative  
933 output, we can approximate the perturbations in the  $\text{PO}_3$ DNN (denoted as  $f(x)$ , where  $x$  is the targeted  
934 sensitivity parameter) using the Taylor expansion:

935  $f(1.1x) \approx f(x) + (1.1x - x)\nabla f(x) = f(x) + 0.1x.\nabla f(x)$  (12)

936  $f(0.9x) \approx f(x) + (0.9x - x)\nabla f(x) = f(x) - 0.1x.\nabla f(x)$  (13)

937 The sensitivity calculation presented in Eq.3 can be rewritten in the following form:

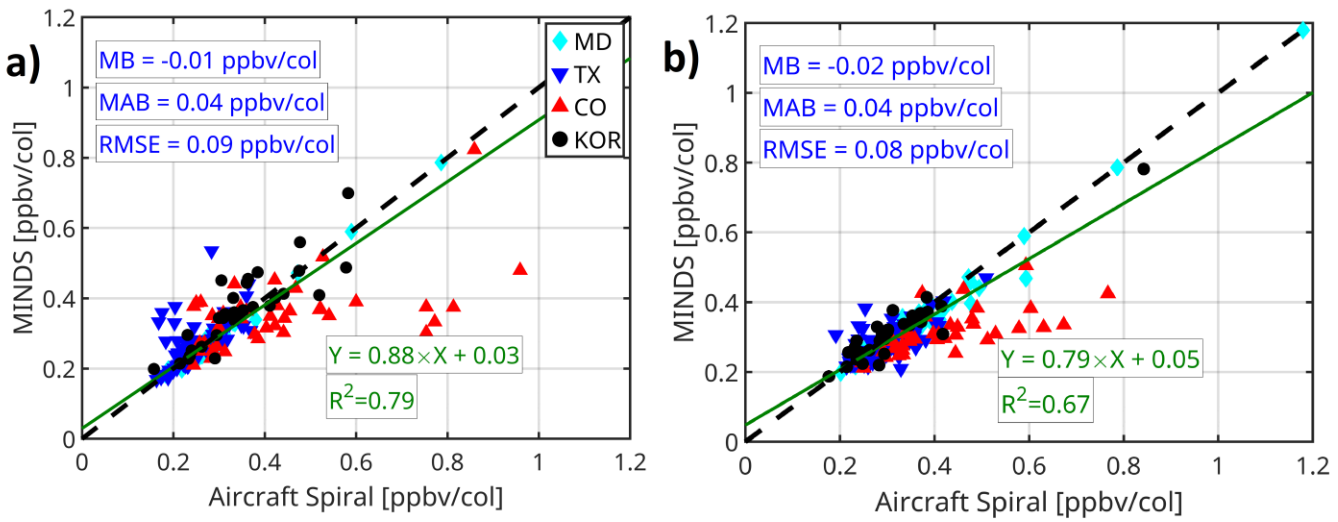
$$S = \frac{(f(x) + 0.1\nabla f(x)) - (f(x) - 0.1\nabla f(x))}{0.2} = \frac{0.2x.\nabla f(x)}{0.2} = x.\nabla f(x) \quad (14)$$

938 Therefore, the first-order approximation of the DNN prediction, when using the given sensitivity  
 939 calculation, is  $x.\nabla f(x)$  which represents the first-order Taylor expansion term that describes how the output  
 940 changes with respect to both the gradient and the magnitude of  $x$  (i.e., directional derivative).

941 **Appendix B. MINDS conversion factor validation**

942 We validate the column conversion factors obtained from the MINDS simulations against  
 943 corresponding values derived from aircraft spirals from several suborbital missions. The concentrations of  
 944 HCHO and NO<sub>2</sub> in both datasets are collocated in time and space and are resampled onto a common vertical  
 945 grid, ranging from the near surface up to 450 hPa in 20 hPa increments. To determine the conversion factors,  
 946 these resampled concentrations are averaged within the PBL and then divided by the vertically integrated  
 947 partial columns from the surface to 450 hPa. The PBLH is based on the MINDS simulations. Figure B.1  
 948 displays scatterplots of the paired conversion factor binned at 12:15 LST and 15:15 LST ( $\pm 45$  minutes  
 949 around the TROPOMI/OMI local revisit time) for NO<sub>2</sub> and HCHO, respectively. The unit for these  
 950 conversion factors is ppbv/col, where col represents  $1 \times 10^{15}$  molec.cm<sup>-2</sup>. The comparison shows a good level  
 951 of agreement between the two datasets for both species ( $R^2 > 0.7$ ). The MINDS simulations perform slightly  
 952 better for NO<sub>2</sub> than for HCHO. This performance difference may arise from the fact that HCHO is mainly  
 953 a secondary product, meaning various uncertain VOC emissions, along with uncertain chemical processes  
 954 in the model, could pile up leading to discrepancies in the vertical distribution of simulated HCHO  
 955 compared to observations. Furthermore, HCHO vertical profiles can be easily affected by local circulation  
 956 patterns that are difficult to resolve in coarse models (Souri et al., 2023b). We observe consistent model  
 957 performance across various campaigns, except for DISCOVER-AQ Colorado. This discrepancy may result  
 958 from complex topography and wind conditions in that region that the model might not fully capture. The  
 959 differences between the two datasets can also be attributed to sources of error beyond the model  
 960 deficiencies. For instance, the MINDS simulations represent a quarter-degree averaged concentration,  
 961 which differs from the localized air samples derived from aircraft, known as the spatial representation error  
 962 (Souri et al., 2022).

963 To account for the systematic errors resulting from the MINDS simulation in our error budget, we  
 964 assign  $e_{conv-HCHO}$  and  $e_{conv-NO2}$  in Eq.5 to RMSE values obtained from the comparison. The choice of RMSE  
 965 is based on the fact that it contains information about the bias and the dispersion of MINDS with respect to  
 966 the observations. We assume these errors to be invariant by time or location, mainly because of limited  
 967 aircraft spirals ( $N=57$ ) we have from the suborbital missions.



96  
 970 **Figure B.1.** The scatterplot of the column to the PBL conversion factor for (a) NO<sub>2</sub> and (b) HCHO obtained  
 971 from aircraft spirals (x-axis) and MINDS simulation (y-axis) at the same time and location from four  
 972 different suborbital missions. These 57 spirals are limited to OMI/TROPOMI overpass  $\pm 45$  min buffering  
 973 time. “col” denotes  $1 \times 10^{15}$  molec.cm<sup>-2</sup>.

974

975 **Financial Support**

976 This study is funded by NASA's ACMAP/Aura project (grant no. 80NSSC23K1250).

977 **Data Availability**

978 The PO<sub>3</sub> products can be obtained from <https://www.ozonerates.space>.

979 TROPOMI satellite data are derived from copernicus Sentinel-5P (processed by ESA), 2021, TROPOMI  
980 Level 2 Nitrogen Dioxide total column products. Version 02. European Space Agency.  
981 <https://doi.org/10.5270/S5P-9bnp8q8>, and copernicus Sentinel-5P (processed by ESA), 2020, TROPOMI  
982 Level 2 Formaldehyde Total Column products. Version 02. European Space Agency.  
983 <https://doi.org/10.5270/S5P-vgl17t0>. The TROPOMI UV DLER can be obtained from  
984 [https://www.temis.nl/surface/albedo/tropomi\\_ler.php](https://www.temis.nl/surface/albedo/tropomi_ler.php) (last access: 10 Nov 2024). OMI SAO HCHO at  
985 [https://waps.cfa.harvard.edu/sao\\_atmos/data/omi\\_hcho/OMI-HCHO-L2/](https://waps.cfa.harvard.edu/sao_atmos/data/omi_hcho/OMI-HCHO-L2/) (last access, 15 Feb 2025).  
986 MINDS simulations can be obtained from [https://portal.nccs.nasa.gov/datasshare/merra2\\_gmi/gmi-minds/](https://portal.nccs.nasa.gov/datasshare/merra2_gmi/gmi-minds/)  
987 (last access, 10 April 2025). OMI NO<sub>2</sub> (QA4ECV) can be downloaded from <https://www.temis.nl/> (last  
988 access, 10 April 2025).

989 **Competing interests**

990 Bryan N. Duncan is a member of the editorial board of Atmospheric Chemistry and Physics

991 **Acknowledgements**

992 Resources supporting this work were provided by the NASA High-End Computing (HEC) Program through  
993 the NASA Center for Climate Simulation (NCCS) at Goddard Space Flight Center.

994 **Authors' contributions**

995 AHS designed and implemented the research idea, analyzed the data, made all figures except for Figures 2  
996 and 3, and wrote the manuscript. GG implemented, designed, and validated the DNN algorithm, and made  
997 Figures 2 and 3. LDM provided the MINDS simulations. BND helped with the interpretation of the results  
998 and editing.

999

1000

1001

1002 **References**

1003 Abadi, M., Barham, P., Chen, J., Chen, Z., Davis, A., Dean, J., Devin, M., Ghemawat, S., Irving, G., Isard, M., Kudlur, M., Levenberg, J., Monga, R., Moore, S., Murray, D. G., Steiner, B., Tucker, P., Vasudevan, V., Warden, P., Wicke, M., Yu, Y., and Zheng, X.: TensorFlow: A system for large-scale machine learning, <https://doi.org/10.48550/arXiv.1605.08695>, 31 May 2016.

1007 Anderson, D. C., Duncan, B. N., Liu, J., Nicely, J. M., Strode, S. A., Follette-Cook, M. B., Souri, A. H., Ziemke, J. R., González-Abad, G., and Ayazpour, Z.: Trends and Interannual Variability of the Hydroxyl Radical in the Remote Tropics During Boreal Autumn Inferred From Satellite Proxy Data, *Geophys. Res. Lett.*, 51, e2024GL108531, <https://doi.org/10.1029/2024GL108531>, 2024.

1011 Ayazpour, Z., González Abad, G., Nowlan, C. R., Sun, K., Kwon, H.-A., Chan Miller, C., Chong, H., Wang, H., Liu, X., Chance, K., O'Sullivan, E., Zhu, L., Vigouroux, C., De Smedt, I., Stremme, W., Hannigan, J. W., Notholt, J., Sun, X., Palm, M., Petri, C., Strong, K., Röhling, A. N., Mahieu, E., Smale, D., Té, Y., Morino, I., Murata, I., Nagahama, T., Kivi, R., Makarova, M., Jones, N., Sussmann, R., and Zhou, M.: Aura Ozone Monitoring Instrument (OMI) Collection 4 Formaldehyde Products, *Earth Space Sci.*, 12, e2024EA003792, <https://doi.org/10.1029/2024EA003792>, 2025.

1018 Bates, K. H. and Jacob, D. J.: An Expanded Definition of the Odd Oxygen Family for Tropospheric Ozone Budgets: Implications for Ozone Lifetime and Stratospheric Influence, *Geophys. Res. Lett.*, 47, e2019GL084486, <https://doi.org/10.1029/2019GL084486>, 2020.

1021 Bauwens, M., Stavrakou, T., Müller, J.-F., De Smedt, I., Van Roozendael, M., van der Werf, G. R., Wiedinmyer, C., Kaiser, J. W., Sindelarova, K., and Guenther, A.: Nine years of global hydrocarbon emissions based on source inversion of OMI formaldehyde observations, *Atmos. Chem. Phys.*, 16, 10133–10158, <https://doi.org/10.5194/acp-16-10133-2016>, 2016.

1025 Bocquet, M., Elbern, H., Eskes, H., Hirtl, M., Žabkar, R., Carmichael, G. R., Flemming, J., Inness, A., Pagowski, M., Pérez Camaño, J. L., Saide, P. E., San Jose, R., Sofiev, M., Vira, J., Baklanov, A., Carnevale, C., Grell, G., and Seigneur, C.: Data assimilation in atmospheric chemistry models: current status and future prospects for coupled chemistry meteorology models, *Atmos. Chem. Phys.*, 15, 5325–5358, <https://doi.org/10.5194/acp-15-5325-2015>, 2015.

1030 Boersma, K. F., Eskes, H. J., Richter, A., De Smedt, I., Lorente, A., Beirle, S., van Geffen, J. H. G. M., Zara, M., Peters, E., Van Roozendael, M., Wagner, T., Maasakkers, J. D., van der A, R. J., Nightingale, J., De Rudder, A., Irie, H., Pinardi, G., Lambert, J.-C., and Compernolle, S. C.: Improving algorithms and uncertainty estimates for satellite NO<sub>2</sub> retrievals: results from the quality assurance for the essential climate variables (QA4ECV) project, *Atmos. Meas. Tech.*, 11, 6651–6678, <https://doi.org/10.5194/amt-11-6651-2018>, 2018.

1036 Boynard, A., Wespes, C., Hadji-Lazaro, J., Sinnathamby, S., Hurtmans, D., Coheur, P.-F., Douriaux-Boucher, M., Onderwaater, J., Steinbrecht, W., Pennington, E. A., Bowman, K., and Clerbaux, C.: Assessment of 16-year tropospheric ozone trends from the IASI Climate Data Record, *Atmos. Chem. Phys.*, 25, 11719–11755, <https://doi.org/10.5194/acp-25-11719-2025>, 2025.

1040 Borger, C., Beirle, S., and Wagner, T.: Analysis of global trends of total column water vapour from multiple years of OMI observations, *Atmos. Chem. Phys.*, 22, 10603–10621, <https://doi.org/10.5194/acp-22-10603-2022>, 2022.

1043 Brune, W. H., Miller, D. O., Thames, A. B., Allen, H. M., Apel, E. C., Blake, D. R., Bui, T. P., Commane, R., Crounse, J. D., Daube, B. C., Diskin, G. S., DiGangi, J. P., Elkins, J. W., Hall, S. R., Hanisco, T. F., Hannun, R. A., Hinsta, E. J., Hornbrook, R. S., Kim, M. J., McKain, K., Moore, F. L., Neuman, J. A., Nicely, J. M., Peischl, J., Ryerson, T. B., St. Clair, J. M., Sweeney, C., Teng, A. P., Thompson,

1047 C., Ullmann, K., Veres, P. R., Wennberg, P. O., and Wolfe, G. M.: Exploring Oxidation in the  
1048 Remote Free Troposphere: Insights From Atmospheric Tomography (ATom), *J. Geophys. Res.-*  
1049 *Atmos.*, 125, e2019JD031685, <https://doi.org/10.1029/2019JD031685>, 2020.

1050 Brune, W. H., Miller, D. O., Thames, A. B., Brosius, A. L., Barletta, B., Blake, D. R., Blake, N. J., Chen,  
1051 G., Choi, Y., Crawford, J. H., Digangi, J. P., Diskin, G., Fried, A., Hall, S. R., Hanisco, T. F., Huey,  
1052 G. L., Hughes, S. C., Kim, M., Meinardi, S., Montzka, D. D., Pusede, S. E., Schroeder, J. R., Teng,  
1053 A., Tanner, D. J., Ullmann, K., Walega, J., Weinheimer, A., Wisthaler, A., and Wennberg, P. O.:  
1054 Observations of atmospheric oxidation and ozone production in South Korea, *Atmos. Environ.*,  
1055 269, 118854, <https://doi.org/10.1016/j.atmosenv.2021.118854>, 2022.

1056 Cazorla, M. and Brune, W. H.: Measurement of Ozone Production Sensor, *Atmos. Meas. Tech.*, 3, 545–555,  
1057 <https://doi.org/10.5194/amt-3-545-2010>, 2010.

1058 Cazorla, M., Brune, W. H., Ren, X., and Lefer, B.: Direct measurement of ozone production rates in Houston  
1059 in 2009 and comparison with two estimation methods, *Atmos. Chem. Phys.*, 12, 1203–1212,  
1060 <https://doi.org/10.5194/acp-12-1203-2012>, 2012.

1061 Chatfield, R. B., Ren, X., Brune, W., and Schwab, J.: Controls on urban ozone production rate as indicated  
1062 by formaldehyde oxidation rate and nitric oxide, *Atmos. Environ.*, 44, 5395–5406,  
1063 <https://doi.org/10.1016/j.atmosenv.2010.08.056>, 2010.

1064 Chin, M., Ginoux, P., Kinne, S., Torres, O., Holben, B. N., Duncan, B. N., Martin, R. V., Logan, J. A.,  
1065 Higurashi, A., and Nakajima, T.: Tropospheric Aerosol Optical Thickness from the GOCART  
1066 Model and Comparisons with Satellite and Sun Photometer Measurements, *J. Atmos. Sci.*, 59, 461–  
1067 483, [https://doi.org/10.1175/1520-0469\(2002\)059<0461:TAOTFT>2.0.CO;2](https://doi.org/10.1175/1520-0469(2002)059<0461:TAOTFT>2.0.CO;2), 2002.

1068 Choi, Y. and Souri, A. H.: Chemical condition and surface ozone in large cities of Texas during the last  
1069 decade: Observational evidence from OMI, CAMS, and model analysis, *Remote Sens. Environ.*,  
1070 168, 90–101, <https://doi.org/10.1016/j.rse.2015.06.026>, 2015a.

1071 Choi, Y. and Souri, A. H.: Seasonal behavior and long-term trends of tropospheric ozone, its precursors and  
1072 chemical conditions over Iran: A view from space, *Atmos. Environ.*, 106, 232–240,  
1073 <https://doi.org/10.1016/j.atmosenv.2015.02.012>, 2015b.

1074 Choi, Y., Kim, H., Tong, D., and Lee, P.: Summertime weekly cycles of observed and modeled NO<sub>x</sub> and  
1075 O<sub>3</sub> concentrations as a function of satellite-derived ozone production sensitivity and land use types  
1076 over the Continental United States, *Atmos. Chem. Phys.*, 12, 6291–6307,  
1077 <https://doi.org/10.5194/acp-12-6291-2012>, 2012.

1078 Compernolle, S., Verhoelst, T., Pinardi, G., Granville, J., Hubert, D., Keppens, A., Niemeijer, S., Rino, B.,  
1079 Bais, A., Beirle, S., Boersma, F., Burrows, J. P., De Smedt, I., Eskes, H., Goutail, F., Hendrick, F.,  
1080 Lorente, A., Pazmino, A., Piters, A., Peters, E., Pommereau, J.-P., Remmers, J., Richter, A., van  
1081 Geffen, J., Van Roozendael, M., Wagner, T., and Lambert, J.-C.: Validation of Aura-OMI QA4ECV  
1082 NO<sub>2</sub> climate data records with ground-based DOAS networks: the role of measurement and  
1083 comparison uncertainties, *Atmos. Chem. Phys.*, 20, 8017–8045, <https://doi.org/10.5194/acp-20-8017-2020>, 2020.

1085 Cooper, M. J., Martin, R. V., McLinden, C. A., and Brook, J. R.: Inferring ground-level nitrogen dioxide  
1086 concentrations at fine spatial resolution applied to the TROPOMI satellite instrument, *Environ.*  
1087 *Res. Lett.*, 15, 104013, <https://doi.org/10.1088/1748-9326/aba3a5>, 2020.

1088

1089 David, L. M. and Nair, P. R.: Tropospheric column O<sub>3</sub> and NO<sub>2</sub> over the Indian region observed by Ozone  
1090 Monitoring Instrument (OMI): Seasonal changes and long-term trends, *Atmos. Environ.*, 65, 25–  
1091 39, <https://doi.org/10.1016/j.atmosenv.2012.09.033>, 2013.

1092 De Smedt, I., Pinardi, G., Vigouroux, C., Compernolle, S., Bais, A., Benavent, N., Boersma, F., Chan, K.-  
1093 L., Donner, S., Eichmann, K.-U., Hedelt, P., Hendrick, F., Irie, H., Kumar, V., Lambert, J.-C.,  
1094 Langerock, B., Lerot, C., Liu, C., Loyola, D., Piters, A., Richter, A., Rivera Cárdenas, C., Romahn,  
1095 F., Ryan, R. G., Sinha, V., Theys, N., Vlietinck, J., Wagner, T., Wang, T., Yu, H., and Van  
1096 Roozendael, M.: Comparative assessment of TROPOMI and OMI formaldehyde observations and  
1097 validation against MAX-DOAS network column measurements, *Atmos. Chem. Phys.*, 21, 12561–  
1098 12593, <https://doi.org/10.5194/acp-21-12561-2021>, 2021.

1099 Duncan, B. N., Strahan, S. E., Yoshida, Y., Steenrod, S. D., and Livesey, N.: Model study of the cross-  
1100 tropopause transport of biomass burning pollution, *Atmos. Chem. Phys.*, 7, 3713–3736,  
1101 <https://doi.org/10.5194/acp-7-3713-2007>, 2007.

1102 Duncan, B., Y. Yoshida, J. Olson, S. Sillman, C. Retscher, R. Martin, L. Lamsal, Y. Hu, K. Pickering, C.  
1103 Retscher, D. Allen, and J. Crawford, Application of OMI observations to a space-based indicator  
1104 of NO<sub>x</sub> and VOC controls on surface ozone formation, *Atmos. Environ.*, 44, 2213–2223,  
1105 <https://doi.org/10.1016/j.atmosenv.2010.03.010>, 2010.

1106 Eskes, H. J. and Boersma, K. F.: Averaging kernels for DOAS total-column satellite retrievals, *Atmos.*  
1107 *Chem. Phys.*, 3, 1285–1291, <https://doi.org/10.5194/acp-3-1285-2003>, 2003.

1108 Fisher, B. L., Lamsal, L. N., Fasnacht, Z., Oman, L. D., Joiner, J., Krotkov, N. A., Choi, S., Qin, W., and  
1109 Yang, E.-S.: Revised estimates of NO<sub>2</sub> reductions during the COVID-19 lockdowns using updated  
1110 TROPOMI NO<sub>2</sub> retrievals and model simulations, *Atmos. Environ.*, 326, 120459,  
1111 <https://doi.org/10.1016/j.atmosenv.2024.120459>, 2024.

1112 Fleming, Z. L., Doherty, R. M., von Schneidemesser, E., Malley, C. S., Cooper, O. R., Pinto, J. P., Colette,  
1113 A., Xu, X., Simpson, D., Schultz, M. G., Lefohn, A. S., Hamad, S., Moolla, R., Solberg, S., and  
1114 Feng, Z.: Tropospheric Ozone Assessment Report: Present-day ozone distribution and trends  
1115 relevant to human health, *Elem. Sci. Anth.*, 6, 12, <https://doi.org/10.1525/elementa.273>, 2018.

1116 Gaudel, A., Cooper, O. R., Ancellet, G., Barret, B., Boynard, A., Burrows, J. P., Clerbaux, C., Coheur, P.-  
1117 F., Cuesta, J., Cuevas, E., Doniki, S., Dufour, G., Ebojie, F., Foret, G., Garcia, O., Granados-Muñoz,  
1118 M. J., Hannigan, J. W., Hase, F., Hassler, B., Huang, G., Hurtmans, D., Jaffe, D., Jones, N.,  
1119 Kalabokas, P., Kerridge, B., Kulawik, S., Latter, B., Leblanc, T., Le Flochmoën, E., Lin, W., Liu,  
1120 J., Liu, X., Mahieu, E., McClure-Begley, A., Neu, J. L., Osman, M., Palm, M., Petetin, H.,  
1121 Petropavlovskikh, I., Querel, R., Rahpoe, N., Rozanov, A., Schultz, M. G., Schwab, J., Siddans, R.,  
1122 Smale, D., Steinbacher, M., Tanimoto, H., Tarasick, D. W., Thouret, V., Thompson, A. M., Trickl,  
1123 T., Weatherhead, E., Wespes, C., Worden, H. M., Vigouroux, C., Xu, X., Zeng, G., and Ziemke, J.:  
1124 Tropospheric Ozone Assessment Report: Present-day distribution and trends of tropospheric ozone  
1125 relevant to climate and global atmospheric chemistry model evaluation, *Elem. Sci. Anth.*, 6, 39,  
1126 <https://doi.org/10.1525/elementa.291>, 2018.

1127 Georgoulias, A. K., Boersma, K. F., van Vliet, J., Zhang, X., van der A, R., Zanis, P., and de Laat, J.:  
1128 Detection of NO<sub>2</sub> pollution plumes from individual ships with the TROPOMI/S5P satellite sensor,  
1129 *Environ. Res. Lett.*, 15, 124037, <https://doi.org/10.1088/1748-9326/abc445>, 2020.

1130 Gonzalez Abad, G., Souri, A. H., Bak, J., Chance, K., Flynn, L. E., Krotkov, N. A., Lamsal, L., Li, C., Liu,  
1131 X., Miller, C. C., Nowlan, C. R., Suleiman, R., and Wang, H.: Five decades observing Earth's  
1132 atmospheric trace gases using ultraviolet and visible backscatter solar radiation from space, *J.*  
1133 *Quant. Spectrosc. Ra.*, 238, 106478, <https://doi.org/10.1016/j.jqsrt.2019.04.030>, 2019.

1134 Granier, C., Bessagnet, B., Bond, T., D'Angiola, A., Denier van der Gon, H., Frost, G. J., Heil, A., Kaiser,  
1135 J. W., Kinne, S., Klimont, Z., Kloster, S., Lamarque, J.-F., Liousse, C., Masui, T., Meleux, F.,  
1136 Mieville, A., Ohara, T., Raut, J.-C., Riahi, K., Schultz, M. G., Smith, S. J., Thompson, A., van  
1137 Aardenne, J., van der Werf, G. R., and van Vuuren, D. P.: Evolution of anthropogenic and biomass  
1138 burning emissions of air pollutants at global and regional scales during the 1980–2010 period, *Clim.  
1139 Change*, 109, 163, <https://doi.org/10.1007/s10584-011-0154-1>, 2011.

1140 Guenther, A. B., Jiang, X., Heald, C. L., Sakulyanontvittaya, T., Duhl, T., Emmons, L. K., and Wang, X.:  
1141 The Model of Emissions of Gases and Aerosols from Nature version 2.1 (MEGAN2.1): an extended  
1142 and updated framework for modeling biogenic emissions, *Geosci. Model Dev.*, 5, 1471–1492,  
1143 <https://doi.org/10.5194/gmd-5-1471-2012>, 2012.

1144 Hilboll, A., Richter, A., and Burrows, J. P.: Long-term changes of tropospheric NO<sub>2</sub> over megacities derived  
1145 from multiple satellite instruments, *Atmos. Chem. Phys.*, 13, 4145–4169,  
1146 <https://doi.org/10.5194/acp-13-4145-2013>, 2013.

1147 Ichoku, C. and Ellison, L.: Global top-down smoke-aerosol emissions estimation using satellite fire  
1148 radiative power measurements, *Atmos. Chem. Phys.*, 14, 6643–6667, <https://doi.org/10.5194/acp-14-6643-2014>, 2014.

1149 Jeon, W., Choi, Y., Souri, A. H., Roy, A., Diao, L., Pan, S., Lee, H. W., and Lee, S.-H.: Identification of  
1150 chemical fingerprints in long-range transport of burning induced upper tropospheric ozone from  
1151 Colorado to the North Atlantic Ocean, *Sci. Total Environ.*, 613–614, 820–828,  
1152 <https://doi.org/10.1016/j.scitotenv.2017.09.177>, 2018.

1153 Jin, X., Fiore, A. M., Murray, L. T., Valin, L. C., Lamsal, L. N., Duncan, B., Folkert Boersma, K., De Smedt,  
1154 I., Abad, G. G., Chance, K., and Tonnesen, G. S.: Evaluating a Space-Based Indicator of Surface  
1155 Ozone-NO<sub>x</sub>-VOC Sensitivity Over Midlatitude Source Regions and Application to Decadal  
1156 Trends, *J. Geophys. Res.-Atmos.*, 122, 10,439–10,461, <https://doi.org/10.1002/2017JD026720>,  
1157 2017.

1158 Johnson, M. S., Philip, S., Meech, S., Kumar, R., Sorek-Hamer, M., Shiga, Y. P., and Jung, J.: Insights into  
1159 the long-term (2005–2021) spatiotemporal evolution of summer ozone production sensitivity in the  
1160 Northern Hemisphere derived with the Ozone Monitoring Instrument (OMI), *Atmos. Chem. Phys.*,  
1161 24, 10363–10384, <https://doi.org/10.5194/acp-24-10363-2024>, 2024.

1162 Kingma, D. P. and Ba, J.: Adam: A Method for Stochastic Optimization,  
1163 <https://doi.org/10.48550/arXiv.1412.6980>, 30 January 2017.

1164 Kleinman, L. I., Daum, P. H., Imre, D., Lee, Y.-N., Nunnermacker, L. J., Springston, S. R., Weinstein-Lloyd,  
1165 J., and Rudolph, J.: Ozone production rate and hydrocarbon reactivity in 5 urban areas: A cause of  
1166 high ozone concentration in Houston, *Geophys. Res. Lett.*, 29, 105-1-105-4,  
1167 <https://doi.org/10.1029/2001GL014569>, 2002.

1168 Kleinman, L. I., Daum, P. H., Lee, Y.-N., Nunnermacker, L. J., Springston, S. R., Weinstein-Lloyd, J., and  
1169 Rudolph, J.: A comparative study of ozone production in five U.S. metropolitan areas, *J. Geophys.  
1170 Res.-Atmos.*, 110, <https://doi.org/10.1029/2004JD005096>, 2005.

1171 Martin, R. V., Fiore, A. M., and Van Donkelaar, A.: Space-based diagnosis of surface ozone sensitivity to  
1172 anthropogenic emissions, *Geophys. Res. Lett.*, 31, <https://doi.org/10.1029/2004GL019416>, 2004.

1173 Mazzuca, G. M., Ren, X., Loughner, C. P., Estes, M., Crawford, J. H., Pickering, K. E., Weinheimer, A. J.,  
1174 and Dickerson, R. R.: Ozone production and its sensitivity to NO<sub>x</sub> and VOCs: results from the  
1175 DISCOVER-AQ field experiment, Houston 2013, *Atmos. Chem. Phys.*, 16, 14463–14474,  
1176 <https://doi.org/10.5194/acp-16-14463-2016>, 2016.

1177

1178 Miller, D. O. and Brune, W. H.: Investigating the Understanding of Oxidation Chemistry Using 20 Years of  
1179 Airborne OH and HO<sub>2</sub> Observations, *J. Geophys. Res.-Atmos.*, 127, e2021JD035368,  
1180 <https://doi.org/10.1029/2021JD035368>, 2022.

1181 Mills, G., Pleijel, H., Malley, C. S., Sinha, B., Cooper, O. R., Schultz, M. G., Neufeld, H. S., Simpson, D.,  
1182 Sharps, K., Feng, Z., Gerosa, G., Harmens, H., Kobayashi, K., Saxena, P., Paoletti, E., Sinha, V.,  
1183 and Xu, X.: Tropospheric Ozone Assessment Report: Present-day tropospheric ozone distribution  
1184 and trends relevant to vegetation, *Elem. Sci. Anth.*, 6, 47, <https://doi.org/10.1525/elementa.302>,  
1185 2018.

1186 Miyazaki, K., Bowman, K. W., Yumimoto, K., Walker, T., and Sudo, K.: Evaluation of a multi-model, multi-  
1187 constituent assimilation framework for tropospheric chemical reanalysis, *Atmos. Chem. Phys.*, 20,  
1188 931–967, <https://doi.org/10.5194/acp-20-931-2020>, 2020.

1189 Molod, A., Takacs, L., Suarez, M., and Bacmeister, J.: Development of the GEOS-5 atmospheric general  
1190 circulation model: evolution from MERRA to MERRA2, *Geosci. Model Dev.*, 8, 1339–1356,  
1191 <https://doi.org/10.5194/gmd-8-1339-2015>, 2015.

1192 Nielsen, J. E., Pawson, S., Molod, A., Auer, B., da Silva, A. M., Douglass, A. R., Duncan, B., Liang, Q.,  
1193 Manyin, M., Oman, L. D., Putman, W., Strahan, S. E., and Wargan, K.: Chemical Mechanisms and  
1194 Their Applications in the Goddard Earth Observing System (GEOS) Earth System Model, *J. Adv.*  
1195 *Model. Earth Syst.*, 9, 3019–3044, <https://doi.org/10.1002/2017MS001011>, 2017.

1196 Nowlan, C. R., González Abad, G., Kwon, H.-A., Ayazpour, Z., Chan Miller, C., Chance, K., Chong, H.,  
1197 Liu, X., O’Sullivan, E., Wang, H., Zhu, L., De Smedt, I., Jaross, G., Seftor, C., and Sun, K.: Global  
1198 Formaldehyde Products From the Ozone Mapping and Profiler Suite (OMPS) Nadir Mappers on  
1199 Suomi NPP and NOAA-20, *Earth Space Sci.*, 10, e2022EA002643,  
1200 <https://doi.org/10.1029/2022EA002643>, 2023.

1201 Opacka, B., Stavrakou, T., Müller, J.-F., De Smedt, I., van Geffen, J., Marais, E. A., Horner, R. P., Millet,  
1202 D. B., Wells, K. C., and Guenther, A. B.: Natural emissions of VOC and NO<sub>x</sub> over Africa  
1203 constrained by TROPOMI HCHO and NO<sub>2</sub> data using the MAGRITTEv1.1 model, *Atmos. Chem.*  
1204 *Phys.*, 25, 2863–2894, <https://doi.org/10.5194/acp-25-2863-2025>, 2025.

1205 Orbe, C., Oman, L. D., Strahan, S. E., Waugh, D. W., Pawson, S., Takacs, L. L., and Molod, A. M.: Large-  
1206 Scale Atmospheric Transport in GEOS Replay Simulations, *J. Adv. Model. Earth Syst.*, 9, 2545–  
1207 2560, <https://doi.org/10.1002/2017MS001053>, 2017.

1208 Pinardi, G., Van Roozendael, M., Hendrick, F., Theys, N., Abuhassan, N., Bais, A., Boersma, F., Cede, A.,  
1209 Chong, J., Donner, S., Drosoglou, T., Dzhola, A., Eskes, H., Frieß, U., Granville, J., Herman, J. R.,  
1210 Holla, R., Hovila, J., Irie, H., Kanaya, Y., Karagkiozidis, D., Kouremeti, N., Lambert, J.-C., Ma, J.,  
1211 Peters, E., Piters, A., Postlyakov, O., Richter, A., Remmers, J., Takashima, H., Tiefengrab, M.,  
1212 Valks, P., Vlemmix, T., Wagner, T., and Wittrock, F.: Validation of tropospheric NO<sub>2</sub> column  
1213 measurements of GOME-2A and OMI using MAX-DOAS and direct sun network observations,  
1214 *Atmos. Meas. Tech.*, 13, 6141–6174, <https://doi.org/10.5194/amt-13-6141-2020>, 2020.

1215 Ren, X., van Duin, D., Cazorla, M., Chen, S., Mao, J., Zhang, L., Brune, W. H., Flynn, J. H., Grossberg,  
1216 N., Lefer, B. L., Rappenglück, B., Wong, K. W., Tsai, C., Stutz, J., Dibb, J. E., Thomas Jobson, B.,  
1217 Luke, W. T., and Kelley, P.: Atmospheric oxidation chemistry and ozone production: Results from  
1218 SHARP 2009 in Houston, Texas, *J. Geophys. Res.-Atmos.*, 118, 5770–5780,  
1219 <https://doi.org/10.1002/jgrd.50342>, 2013.

1220 Roberts, G., Wooster, M. J., and Lagoudakis, E.: Annual and diurnal african biomass burning temporal  
1221 dynamics, *Biogeosciences*, 6, 849–866, <https://doi.org/10.5194/bg-6-849-2009>, 2009.

1222 Sadanaga, Y., Kawasaki, S., Tanaka, Y., Kajii, Y., and Bandow, H.: New System for Measuring the  
1223 Photochemical Ozone Production Rate in the Atmosphere, *Environ. Sci. Technol.*, 51, 2871–2878,  
1224 <https://doi.org/10.1021/acs.est.6b04639>, 2017.

1225 Schroeder, J. R., Crawford, J. H., Ahn, J.-Y., Chang, L., Fried, A., Walega, J., Weinheimer, A., Montzka, D.  
1226 D., Hall, S. R., Ullmann, K., Wisthaler, A., Mikoviny, T., Chen, G., Blake, D. R., Blake, N. J.,  
1227 Hughes, S. C., Meinardi, S., Diskin, G., Digangi, J. P., Choi, Y., Pusede, S. E., Huey, G. L., Tanner,  
1228 D. J., Kim, M., and Wennberg, P.: Observation-based modeling of ozone chemistry in the Seoul  
1229 metropolitan area during the Korea-United States Air Quality Study (KORUS-AQ), *Elem. Sci.  
1230 Anth.*, 8, 3, <https://doi.org/10.1525/elementa.400>, 2020.

1231 Schroeder, J. R., Crawford, J. H., Fried, A., Walega, J., Weinheimer, A., Wisthaler, A., Müller, M.,  
1232 Mikoviny, T., Chen, G., Shook, M., Blake, D. R., and Tonnesen, G. S.: New insights into the column  
1233 CH<sub>2</sub>O/NO<sub>2</sub> ratio as an indicator of near-surface ozone sensitivity, *J. Geophys. Res.-Atmos.*, 122,  
1234 8885–8907, <https://doi.org/10.1002/2017JD026781>, 2017.

1235 Shen, Z., Yang, H., and Zhang, S.: Neural network approximation: Three hidden layers are enough, *Neural  
1236 Netw.*, 141, 160–173, <https://doi.org/10.1016/j.neunet.2021.04.011>, 2021.

1237 Sillman, S. and He, D.: Some theoretical results concerning O<sub>3</sub>-NO<sub>x</sub>-VOC chemistry and NO<sub>x</sub>-VOC  
1238 indicators, *J. Geophys. Res.-Atmos.*, 107, ACH 26-1-ACH 26-15,  
1239 <https://doi.org/10.1029/2001JD001123>, 2002.

1240 Sklaveniti, S., Locoge, N., Stevens, P. S., Wood, E., Kundu, S., and Dusanter, S.: Development of an  
1241 instrument for direct ozone production rate measurements: measurement reliability and current  
1242 limitations, *Atmos. Meas. Tech.*, 11, 741–761, <https://doi.org/10.5194/amt-11-741-2018>, 2018.

1243 Souri, A. and Gonzalez Abad, G. (2025) “ahsouri/ozonerates: Ozonerates v1.0”. Zenodo. doi:  
1244 10.5281/zenodo.15076487.

1245 Souri, A. H., Chance, K., Sun, K., Liu, X., and Johnson, M. S.: Dealing with spatial heterogeneity in  
1246 pointwise-to-gridded- data comparisons, *Atmos. Meas. Tech.*, 15, 41–59,  
1247 <https://doi.org/10.5194/amt-15-41-2022>, 2022.

1248 Souri, A. H., Choi, Y., Jeon, W., Li, X., Pan, S., Diao, L., and Westenbarger, D. A.: Constraining NO<sub>x</sub>  
1249 emissions using satellite NO<sub>2</sub> measurements during 2013 DISCOVER-AQ Texas campaign,  
1250 *Atmos. Environ.*, 131, 371–381, <https://doi.org/10.1016/j.atmosenv.2016.02.020>, 2016.

1251 Souri, A. H., Choi, Y., Jeon, W., Woo, J.-H., Zhang, Q., and Kurokawa, J.: Remote sensing evidence of  
1252 decadal changes in major tropospheric ozone precursors over East Asia, *J. Geophys. Res.-Atmos.*,  
1253 122, 2474–2492, <https://doi.org/10.1002/2016JD025663>, 2017.

1254 Souri, A. H., Duncan, B. N., Strode, S. A., Anderson, D. C., Manyin, M. E., Liu, J., Oman, L. D., Zhang,  
1255 Z., and Weir, B.: Enhancing long-term trend simulation of the global tropospheric hydroxyl (TOH)  
1256 and its drivers from 2005 to 2019: a synergistic integration of model simulations and satellite  
1257 observations, *Atmos. Chem. Phys.*, 24, 8677–8701, <https://doi.org/10.5194/acp-24-8677-2024>,  
1258 2024.

1259 Souri, A. H., González Abad, G., Wolfe, G. M., Verhoelst, T., Vigouroux, C., Pinardi, G., Compernolle, S.,  
1260 Langerock, B., Duncan, B. N., and Johnson, M. S.: Feasibility of robust estimates of ozone  
1261 production rates using a synergy of satellite observations, ground-based remote sensing, and  
1262 models, *Atmos. Chem. Phys.*, 25, 2061–2086, <https://doi.org/10.5194/acp-25-2061-2025>, 2025.

1263 Souri, A. H., Johnson, M. S., Wolfe, G. M., Crawford, J. H., Fried, A., Wisthaler, A., Brune, W. H., Blake,  
1264 D. R., Weinheimer, A. J., Verhoelst, T., Compernolle, S., Pinardi, G., Vigouroux, C., Langerock,

1265 B., Choi, S., Lamsal, L., Zhu, L., Sun, S., Cohen, R. C., Min, K.-E., Cho, C., Philip, S., Liu, X.,  
1266 and Chance, K.: Characterization of errors in satellite-based HCHO/NO<sub>2</sub> tropospheric column ratios  
1267 with respect to chemistry, column-to-PBL translation, spatial representation, and retrieval  
1268 uncertainties, *Atmos. Chem. Phys.*, 23, 1963–1986, <https://doi.org/10.5194/acp-23-1963-2023>,  
1269 2023a.

1270 Souri, A. H., Kumar, R., Chong, H., Golbazi, M., Knowland, K. E., Geddes, J., and Johnson, M. S.:  
1271 Decoupling in the vertical shape of HCHO during a sea breeze event: The effect on trace gas  
1272 satellite retrievals and column-to-surface translation, *Atmos. Environ.*, 309, 119929,  
1273 <https://doi.org/10.1016/j.atmosenv.2023.119929>, 2023b.

1274 Souri, A. H., Nowlan, C. R., González Abad, G., Zhu, L., Blake, D. R., Fried, A., Weinheimer, A. J.,  
1275 Wisthaler, A., Woo, J.-H., Zhang, Q., Chan Miller, C. E., Liu, X., and Chance, K.: An inversion of  
1276 NO<sub>x</sub> and non-methane volatile organic compound (NMVOC) emissions using satellite observations  
1277 during the KORUS-AQ campaign and implications for surface ozone over East Asia, *Atmos. Chem. Phys.*, 20, 9837–9854, <https://doi.org/10.5194/acp-20-9837-2020>, 2020b.

1279 Souri, A. H., Nowlan, C. R., Wolfe, G. M., Lamsal, L. N., Chan Miller, C. E., Abad, G. G., Janz, S. J., Fried,  
1280 A., Blake, D. R., Weinheimer, A. J., Diskin, G. S., Liu, X., and Chance, K.: Revisiting the  
1281 effectiveness of HCHO/NO<sub>2</sub> ratios for inferring ozone sensitivity to its precursors using high  
1282 resolution airborne remote sensing observations in a high ozone episode during the KORUS-AQ  
1283 campaign, *Atmos. Environ.*, 224, 117341, <https://doi.org/10.1016/j.atmosenv.2020.117341>, 2020a.

1284 Stavrakou, T., Müller, J.-F., Bauwens, M., De Smedt, I., Lerot, C., Van Roozendael, M., Coheur, P.-F.,  
1285 Clerbaux, C., Boersma, K. F., van der A, R., and Song, Y.: Substantial Underestimation of Post-  
1286 Harvest Burning Emissions in the North China Plain Revealed by Multi-Species Space  
1287 Observations, *Sci. Rep.*, 6, 32307, <https://doi.org/10.1038/srep32307>, 2016.

1288 Stavrakou, T., Müller, J.-F., De Smedt, I., Van Roozendael, M., Kanakidou, M., Vrekoussis, M., Wittrock,  
1289 F., Richter, A., and Burrows, J. P.: The continental source of glyoxal estimated by the synergistic  
1290 use of spaceborne measurements and inverse modelling, *Atmos. Chem. Phys.*, 9, 8431–8446,  
1291 <https://doi.org/10.5194/acp-9-8431-2009>, 2009.

1292 Strahan, S. E., Duncan, B. N., and Hoor, P.: Observationally derived transport diagnostics for the lowermost  
1293 stratosphere and their application to the GMI chemistry and transport model, *Atmos. Chem. Phys.*,  
1294 7, 2435–2445, <https://doi.org/10.5194/acp-7-2435-2007>, 2007.

1295 Sullivan, J. T., McGee, T. J., Stauffer, R. M., Thompson, A. M., Weinheimer, A., Knote, C., Janz, S.,  
1296 Wisthaler, A., Long, R., Szykman, J., Park, J., Lee, Y., Kim, S., Jeong, D., Sanchez, D., Twigg, L.,  
1297 Sunnicht, G., Knepp, T., and Schroeder, J. R.: Taehwa Research Forest: a receptor site for severe  
1298 domestic pollution events in Korea during 2016, *Atmos. Chem. Phys.*, 19, 5051–5067,  
1299 <https://doi.org/10.5194/acp-19-5051-2019>, 2019.

1300 Tao, M., Fiore, A. M., Jin, X., Schiferl, L. D., Commane, R., Judd, L. M., Janz, S., Sullivan, J. T., Miller, P.  
1301 J., Karambelas, A., Davis, S., Tzortziou, M., Valin, L., Whitehill, A., Civerolo, K., and Tian, Y.:  
1302 Investigating Changes in Ozone Formation Chemistry during Summertime Pollution Events over  
1303 the Northeastern United States, *Environ. Sci. Technol.*, 56, 15312–15327,  
1304 <https://doi.org/10.1021/acs.est.2c02972>, 2022.

1305 Thorsen, T. J. and Fu, Q.: CALIPSO-inferred aerosol direct radiative effects: Bias estimates using ground-  
1306 based Raman lidars, *J. Geophys. Res.-Atmos.*, 120, 12,209-12,220,  
1307 <https://doi.org/10.1002/2015JD024095>, 2015.

1308 Tilstra, L. G., de Graaf, M., Trees, V. J. H., Litvinov, P., Dubovik, O., and Stammes, P.: A directional surface  
 1309 reflectance climatology determined from TROPOMI observations, *Atmos. Meas. Tech.*, 17, 2235–  
 1310 2256, <https://doi.org/10.5194/amt-17-2235-2024>, 2024.

1311 Valin, L. C., Russell, A. R., Hudman, R. C., and Cohen, R. C.: Effects of model resolution on the  
 1312 interpretation of satellite NO<sub>2</sub> observations, *Atmos. Chem. Phys.*, 11, 11647–11655,  
 1313 <https://doi.org/10.5194/acp-11-11647-2011>, 2011.

1314 van Geffen, J., Eskes, H., Compernolle, S., Pinardi, G., Verhoelst, T., Lambert, J.-C., Sneep, M., ter Linden,  
 1315 M., Ludewig, A., Boersma, K. F., and Veefkind, J. P.: Sentinel-5P TROPOMI NO<sub>2</sub> retrieval: impact  
 1316 of version v2.2 improvements and comparisons with OMI and ground-based data, *Atmos. Meas.  
 1317 Tech.*, 15, 2037–2060, <https://doi.org/10.5194/amt-15-2037-2022>, 2022.

1318 Veefkind, J. P., Aben, I., McMullan, K., Förster, H., de Vries, J., Otter, G., Claas, J., Eskes, H. J., de Haan,  
 1319 J. F., Kleipool, Q., van Weele, M., Hasekamp, O., Hoogeveen, R., Landgraf, J., Snel, R., Tol, P.,  
 1320 Ingmann, P., Voors, R., Kruizinga, B., Vink, R., Visser, H., and Levelt, P. F.: TROPOMI on the ESA  
 1321 Sentinel-5 Precursor: A GMES mission for global observations of the atmospheric composition for  
 1322 climate, air quality and ozone layer applications, *Remote Sens. Environ.*, 120, 70–83,  
 1323 <https://doi.org/10.1016/j.rse.2011.09.027>, 2012.

1324 Verhoelst, T., Compernolle, S., Pinardi, G., Lambert, J.-C., Eskes, H. J., Eichmann, K.-U., Fjæraa, A. M.,  
 1325 Granville, J., Niemeijer, S., Cede, A., Tiefengraber, M., Hendrick, F., Pazmiño, A., Bais, A.,  
 1326 Bazureau, A., Boersma, K. F., Bognar, K., Dehn, A., Donner, S., Elokhov, A., Gebetsberger, M.,  
 1327 Goutail, F., Grutter de la Mora, M., Gruzdev, A., Gratsea, M., Hansen, G. H., Irie, H., Jepsen, N.,  
 1328 Kanaya, Y., Karagkiozidis, D., Kivi, R., Kreher, K., Levelt, P. F., Liu, C., Müller, M., Navarro  
 1329 Comas, M., Piters, A. J. M., Pommereau, J.-P., Portafaix, T., Prados-Roman, C., Puentedura, O.,  
 1330 Querel, R., Remmers, J., Richter, A., Rimmer, J., Rivera Cárdenas, C., Saavedra de Miguel, L.,  
 1331 Sinyakov, V. P., Stremme, W., Strong, K., Van Roozendael, M., Veefkind, J. P., Wagner, T.,  
 1332 Wittrock, F., Yela González, M., and Zehner, C.: Ground-based validation of the Copernicus  
 1333 Sentinel-5P TROPOMI NO<sub>2</sub> measurements with the NDACC ZSL-DOAS, MAX-DOAS and  
 1334 Pandonia global networks, *Atmos. Meas. Tech.*, 14, 481–510, <https://doi.org/10.5194/amt-14-481-2021>, 2021.

1335

1336 Vigouroux, C., Langerock, B., Bauer Aquino, C. A., Blumenstock, T., Cheng, Z., De Mazière, M., De  
 1337 Smedt, I., Grutter, M., Hannigan, J. W., Jones, N., Kivi, R., Loyola, D., Lutsch, E., Mahieu, E.,  
 1338 Makarova, M., Metzger, J.-M., Morino, I., Murata, I., Nagahama, T., Notholt, J., Ortega, I., Palm,  
 1339 M., Pinardi, G., Röhling, A., Smale, D., Stremme, W., Strong, K., Sussmann, R., Té, Y., van  
 1340 Roozendael, M., Wang, P., and Winkler, H.: TROPOMI–Sentinel-5 Precursor formaldehyde  
 1341 validation using an extensive network of ground-based Fourier-transform infrared stations, *Atmos.  
 1342 Meas. Tech.*, 13, 3751–3767, <https://doi.org/10.5194/amt-13-3751-2020>, 2020.

1343 Vinken, G. C. M., Boersma, K. F., Jacob, D. J., and Meijer, E. W.: Accounting for non-linear chemistry of  
 1344 ship plumes in the GEOS-Chem global chemistry transport model, *Atmos. Chem. Phys.*, 11, 11707–  
 1345 11722, <https://doi.org/10.5194/acp-11-11707-2011>, 2011.

1346 Wolfe, G. M., Hanisco, T. F., Arkinson, H. L., Blake, D. R., Wisthaler, A., Mikoviny, T., Ryerson, T. B.,  
 1347 Pollack, I., Peischl, J., Wennberg, P. O., Crounse, J. D., St. Clair, J. M., Teng, A., Huey, L. G., Liu,  
 1348 X., Fried, A., Weibring, P., Richter, D., Walega, J., Hall, S. R., Ullmann, K., Jimenez, J. L.,  
 1349 Campuzano-Jost, P., Bui, T. P., Diskin, G., Podolske, J. R., Sachse, G., and Cohen, R. C.:  
 1350 Photochemical evolution of the 2013 California Rim Fire: synergistic impacts of reactive  
 1351 hydrocarbons and enhanced oxidants, *Atmos. Chem. Phys.*, 22, 4253–4275,  
 1352 <https://doi.org/10.5194/acp-22-4253-2022>, 2022.

1353 Wolfe, G. M., Marvin, M. R., Roberts, S. J., Travis, K. R., and Liao, J.: The Framework for 0-D Atmospheric  
1354 Modeling (F0AM) v3.1, *Geosci. Model Dev.*, 9, 3309–3319, <https://doi.org/10.5194/gmd-9-3309-2016>, 2016.

1355

1356 Yu, K., Jacob, D. J., Fisher, J. A., Kim, P. S., Marais, E. A., Miller, C. C., Travis, K. R., Zhu, L., Yantosca,  
1357 R. M., Sulprizio, M. P., Cohen, R. C., Dibb, J. E., Fried, A., Mikoviny, T., Ryerson, T. B., Wennberg,  
1358 P. O., and Wisthaler, A.: Sensitivity to grid resolution in the ability of a chemical transport model  
1359 to simulate observed oxidant chemistry under high-isoprene conditions, *Atmos. Chem. Phys.*, 16,  
1360 4369–4378, <https://doi.org/10.5194/acp-16-4369-2016>, 2016.